



## 2 First Alps-wide reconstruction of LGM glacial sediment transport enabled by GPU-accelerated particle tracking

4 Tancrede Pierre Marie Leger<sup>1</sup>, Guillaume Jouvét<sup>1</sup>, Sarah Kamleitner<sup>1,2</sup>, Brandon David Finley<sup>1</sup>, Maxime  
Bernard<sup>1</sup>, Balthazar Allegri<sup>1</sup>, Frédéric Herman<sup>1</sup>, Andreas Vieli<sup>2</sup>, Andreas Henz<sup>2</sup>, Samuel Urs Nussbaumer<sup>2</sup>

6 <sup>1</sup>Institute of Earth Surface Dynamics, University of Lausanne, Lausanne, Switzerland

8 <sup>2</sup>Department of Geography, University of Zürich, Zürich, Switzerland

10 Correspondence: Tancrede P. M. Leger ([tancrede.leger@unil.ch](mailto:tancrede.leger@unil.ch)); personal address: [tankleger@gmail.com](mailto:tankleger@gmail.com)

12 **Abstract.** Reconstructing the transport histories and provenances of glacial sediments and ice-contact  
deposits (e.g. tills, moraines) in formerly glaciated regions remains a major challenge, particularly at icefield-  
14 to ice-sheet scales and over multi-millennial timescales. Yet such reconstructions are central to key questions  
in Quaternary science, including estimates of past glacial erosion rates and sediment fluxes, the role of  
16 subglacial sediment storage in erosion buffering, or the reconstruction of past ice-flow dynamics, ice divides,  
and transfluences. While numerical modelling can enable one to reproduce past glacial sediment transport  
18 via coupling glacier models with Lagrangian particle tracking, this becomes computationally unfeasible over  
large spatial domains and paleo timescales using traditional computing. As a result, no study to date has  
20 simulated glacial sediment transport using large particle numbers (tens of millions) across continental-scale  
icefields such as the European Alps during the Last Glacial Maximum (LGM): a pre-requisite given the  
22 ubiquitous nature of sediments in glacier systems. In this study, we overcome this limitation through a new  
coupling of 3D Lagrangian particle tracking with Graphics-Processing-Units (GPU)-accelerated, high-  
24 resolution glacier simulations based on the deep-learning-enhanced Instructed Glacier Model (IGM). Our  
approach unlocks the ice advection of tens of millions of particles at minimal additional computational cost,  
26 allowing simulations of glacial sediment transport across the European Alps over multi-millennial timescales  
(40-18 ka) and at an unprecedented spatial resolution of 300 m. In doing so, we produce the first Alps-wide  
28 modelling reconstruction of glacial sediment transport during the LGM, using process-based particle seeding  
schemes to represent both subglacial (e.g. abrasion, plucking) and supraglacial (e.g. rockfall, landslides)  
30 sediment sourcing. Results are analysed through complementary ‘sink-to-source’ (deposit provenance) and  
‘source-to-sink’ (potential depositional pathways) analyses, enabling us to reconstruct the LGM glacial  
32 transport of numerous ice-contact deposits and surface lithologies across the Alps. We find that  
supraglacially sourced glacial sediments are typically eroded earlier, experience longer glacier residence  
34 times, and undergo greater cumulative ice-free exposure than those of subglacial origin, with implications  
for the interpretation of cosmogenic nuclide inheritance in glacial deposits. Our new coupled glacier-particle  
36 modelling framework opens avenues for quantitative model-data comparisons using glacial geomorphology  
and provides a powerful tool for reconstructing paleo ice dynamics, sediment provenance, and Quaternary  
38 glacial landscape evolution.



## 40 **1 Introduction**

42 In the early 1800s, pioneering naturalists argued certain sediments found in mountain forelands evidenced  
widespread past glacier expansions, an idea commonly known as the ‘glacier theory’ (e.g. Esmark, 1824;  
44 Venetz, 1830; Agassiz, 1840; Lyell, 1840). Their hypotheses were later validated by investigations  
characterizing deposits emplaced at the lateral, frontal, or subglacial margins of former glaciers, icefields,  
46 and ice sheets (Sugden & John, 1976). These so-called ‘ice-contact deposits’ include erratic boulders,  
lateral and terminal moraines, till units, drumlins, eskers, lineations, and various other glacio-depositional  
48 landforms (Evans & Benn, 2004). Over the last two centuries, glacial geologists have studied these  
features across formerly glaciated landscapes to reconstruct the extent, duration, style, and timing of past  
50 glacier advances and retreats (e.g. Penck & Brückner, 1909; Evans et al., 2006; Ehlers et al., 2011; Davies  
et al., 2012; Clark et al., 2022). In the European Alps, a long tradition of such work has focused on  
52 reconstructing Quaternary glaciations of the Alpine Ice Field (AIF) (e.g. Geikie, 1910; van Husen, 1997;  
Kelly et al., 2004; Preusser et al., 2010, 2011; Graf et al., 2015; Ivy-Ochs, 2015; 2022). Consequently, the  
54 processes of ice-contact sediment deposition and post-depositional disturbance are often well documented  
in many regions.

56

By contrast, the pre-depositional histories of ice-contact deposits are often poorly constrained. The  
58 inaccessibility and complexity of glacial sediment erosion/transport processes challenge empirical  
characterization in modern glacier systems, and even more so in paleo settings (Boulton, 1996). Field  
60 studies attempting to quantify pre-depositional histories in active glacier systems use techniques such as  
mineralogical provenance analyses (e.g. Herman et al., 2015), detrital and *in situ* low-temperature  
62 thermochronology (e.g. Enkelmann & Ehlers, 2015), terrestrial cosmogenic nuclide concentrations (e.g.  
Guillon et al., 2015), morainic soil material’s fingerprinting analysis (e.g. Mohammadi et al., 2024), or  
64 luminescence rock surface burial dating (Margirier et al., 2025). However, these studies are rare, often  
limited to individual deposits or catchments, and difficult to extend to paleo glacier events. As a result, the  
66 provenance, erosion histories, transport distances, durations, and pathways of ice-contact deposits remain  
highly challenging to constrain at larger spatial and temporal scales.

68

Yet understanding glacial sediment erosion/transport history and their provenance is critical for multiple  
70 research questions. Such insights can, for instance, improve estimates of Quaternary glacial erosion rates  
and sediment fluxes, complementing studies of glaciofluvial sediment export dynamics (e.g. Koppes et  
72 al., 2015; Herman et al., 2015; Lane et al., 2017; Overeem et al., 2017; Delaney et al., 2023). They also  
inform mechanisms and timescales of debris cover and subglacial sediment storage, involved in bedrock  
74 shielding and erosion buffering (Delaney & Anderson, 2022). Pre-depositional sediment histories can also  
reveal past ice dynamics, including interactions with topography and the mechanisms of flow

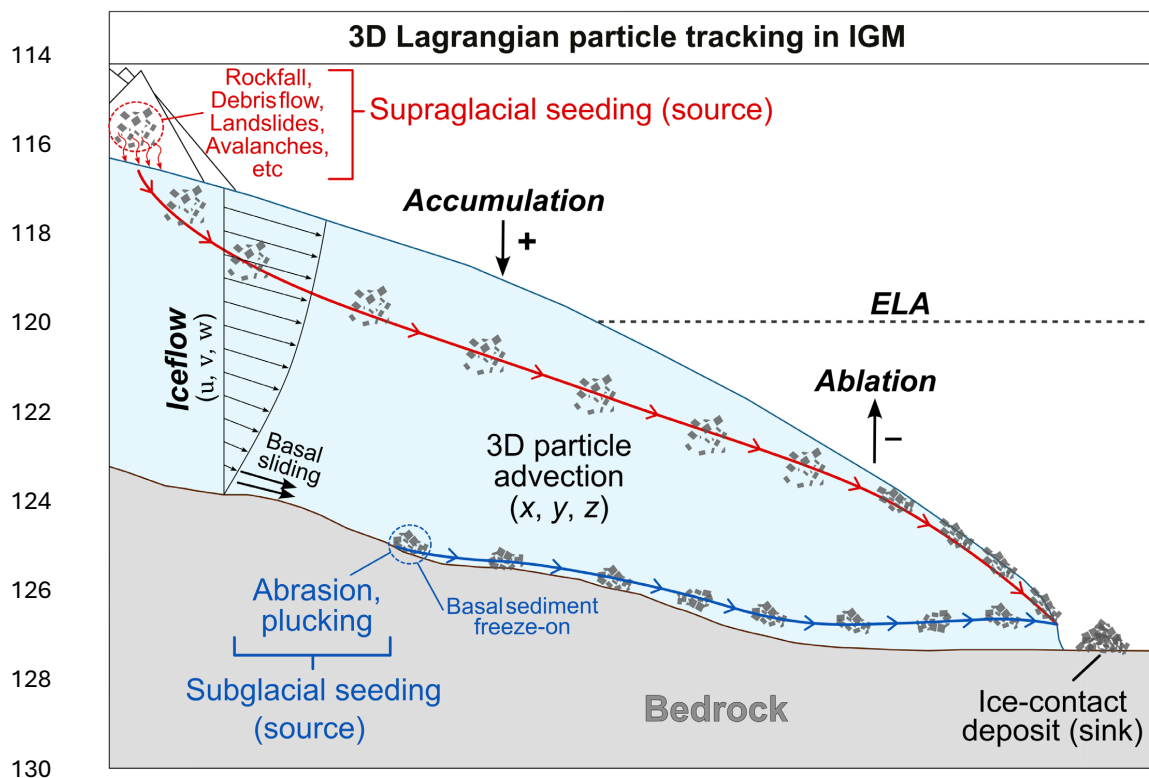


76 convergence/divergence associated with tributary glaciers merging or separating during waxing and  
waning cycles of ice sheets or icefields (Jouvet et al., 2017). These reconstructions aid in identifying  
78 former ice-flow regimes and the position or migration of ice divides, key to interpreting sedimentary  
archives of past ice-flow directionality (e.g. Hughes et al., 2010; Kamleitner et al., 2024) and to mapping  
80 former ice transfluences (e.g. Reitner et al., 2010). Moreover, knowing whether a deposit reached glacier  
ice supraglacially or subglacially, and its glacial transport history, supports the application of  
82 geochronological methods (e.g. cosmogenic exposure or luminescence dating), where prior exposure to  
sunlight or the atmosphere can affect age interpretations (e.g. Heyman et al., 2011). Quantifying glacial  
84 sediment routing and export in formerly glaciated landscapes is also crucial to inform industries for  
instance concerned with aggregate resources or the geological disposal of nuclear waste (Fischer et  
86 al., 2015; 2021). Lastly, tracking the transport history of iconic glacial erratics, some of which have  
cultural significance (Reynard, 2004; Coutterand, 2018), offers an opportunity to bridge scientific  
88 understanding with public engagement. Thus, while it represents a substantial challenge, characterizing  
the pre-depositional history of glacial sediments and ice-contact deposits yields widespread implications  
90 for numerous research fields.

92 Numerical modelling offers a means to address the above knowledge gaps by generating spatially  
distributed, time-evolving estimates of glacial sediment transport which can be compared against  
94 empirical point data (Veness et al., 2025). A robust and established method consists in coupling a  
glacier evolution model with Lagrangian particle tracking to simulate the time-transient advection of  
96 sediment-like particles by ice-flow (e.g. Rybak & Huybrechts, 2003; Rowan et al., 2015; Bernard et al.,  
2020; Scherler & Egholm, 2020). When modelled glacier geometries are somewhat consistent with  
98 empirical evidence, and when particle seeding is parameterised to mimic real sediment erosion processes,  
this method can produce first-order estimates of glacial sediment transport pathways (Margirier et al.,  
100 2025). However, no studies have yet coupled Lagrangian tracking of large particle numbers ( $>10^6$ ) to  
multi-millennial-scale simulations of past Alpine Field (AIF) glaciations. This is largely due to two  
102 constraints. First, previous AIF simulations exhibited potent mismatches in ice thickness compared to field  
data, limiting confidence in inferred ice-flow dynamics (Mey et al., 2016; Seguinot et al., 2018; Jouvet et  
104 al., 2023). Second, standard numerical approaches impose a high computational cost and high memory  
requirement when conducting Lagrangian tracking of large particle numbers: i.e. tens to hundreds of  
106 millions of particles. Given the highly ubiquitous nature of sediments in glacier systems, such high particle  
numbers are essential if one wants to realistically depict some of the natural processes involved (Rowan  
108 et al., 2015). Consequently, no studies to date have simulated glacial sediment transport using large particle  
numbers across continental-scale icefields like the AIF at any timescale, let alone over thousands of years.

110

112



132 Figure 1. Simplified schematic diagram illustrating the Graphics-Processing-Units (GPU) - based, 3D  
133 Lagrangian particle advection scheme of both supraglacially seeded (red) and subglacially seeded (blue)  
134 particles coupled with our Instructed Glacier Model (IGM) setup and implemented in this study. 'ELA'  
135 stands for 'Equilibrium Line Altitude'.

136

138

140

142

144

146

148

150



Here we show that these bottlenecks can be overcome. Leger et al. (2025) produced an ensemble of 100  
152 high-resolution (300 m) simulations of the AIF during the Last Glacial Maximum (LGM), whose best-  
performing simulations improved model-data agreement in both ice thickness and extent compared to  
154 previous efforts (e.g. Seguinot et al., 2018; Jouvét et al., 2023). These advances were enabled by the  
Instructed Glacier Model (IGM), a high-order, thermo-mechanically coupled glacier evolution model  
156 (Jouvét et al., 2021; Jouvét & Cordonnier, 2023). IGM leverages physics-informed machine learning and  
computation on Graphics Processing Units (GPU) to reduce the computational cost of traditional glacier  
158 modelling by several orders of magnitude. Here we show that IGM's novel GPU-based architecture also  
enables efficient parallelization of Lagrangian particle tracking, permitting to couple the advection of  
160 millions of particles within our AIF model framework at minimal additional cost (see Results section) and  
consequently track the glacial-transport trajectories of individual particles from their location of origin  
162 (the source) to their final deposition site (the sink).

164 To this end, we conduct a new set of Alps-wide simulations of the last glaciation of the European Alps  
using the same data-consistent IGM setup as Leger et al. (2025) with the additional coupling of 3D  
166 Lagrangian tracking of large particle numbers. Ultimately, we produce the first Alps-wide model estimates  
of time-transient and 3D glacial sediment trajectories between 40 and 18 ka, the period bracketing the  
168 LGM. We design a new particle advection module and seeding scheme that simulates both the subglacial  
(e.g. via abrasion, plucking) and supraglacial (e.g. via rockfall, debris flow) origins of glacially transported  
170 sediments (Fig. 1). By introducing this new method, we can simulate the complex glacial-transport  
trajectories of LGM ice-contact deposits (e.g. terminal moraines) across the Alps at high spatial (300 m)  
172 and temporal (10 yr) resolutions, and estimate their provenances, glacial transport time, erosion timing,  
and cumulative ice-free time during their source-to-sink journey. With this experiment, we also model the  
174 possible LGM source-to-sink trajectories of certain surface lithologies (i.e. sources) throughout the Alps,  
which we subsequently compare against empirical data on LGM-dated erratics of known location and  
176 lithology (e.g. Kamleitner et al., 2022).

178 The Alps-wide results of this study are presented below and under the form of figure catalogues and  
trajectory shapefiles accessible via the Zenodo repository attached to this paper (link:  
180 <https://doi.org/10.5281/zenodo.18374156>). They provide the means to compare our spatially distributed  
modelling estimates against empirical evidence on, for instance, deposited LGM erratics and their  
182 lithologies/provenance, former ice-flow direction during the LGM, documented ice transfluences, and  
preserved post-retreat deposits and mapped moraines. We believe this first Alps-wide reconstruction of  
184 LGM glacial sediment transport will prove useful to glacial geologists, geomorphologists,  
sedimentologists, and industries studying ice-contact sediments related to the last glaciation of the  
186 European Alps. This new ability to conduct coupled glacier-particle modelling over continental and multi-  
millennial scales opens the door to new model-data comparisons which, in turn, can further improve the





188 accuracy of future AIF models. We provide examples showing how such model estimates can address  
empirical debates and raise new hypotheses that can be tested via future field campaigns. Finally, this  
190 study provides a novel, computationally efficient modelling workflow which opens the possibility to  
produce high-resolution estimates of the erosion, transport, and deposition dynamics of glacial sediments  
192 in numerous glaciated or formerly glaciated regions of the world.

194

## 2 Methods

196

### 2.1 Model setup

198

IGM is a thermo-mechanical 3D glacier evolution model enhanced with physics-informed deep learning  
200 using a convolutional neural network emulator (Jouvet & Cordonnier, 2023) of the high-order  
'Blatter-Pattyn' ice-flow solver (Blatter, 1995). In this study, we build on the results of Leger et al. (2025)  
202 and use the exact same IGM model version (2.2.1), spatial resolution (300 m), input parameters, and  
forcings as used for their ensemble's (n=100) best-scoring simulation, i.e. simulation 37 (see Figs. 1, 6 in  
204 Leger et al., 2025). We also run our simulations using the same GPU (Nvidia RTX 4090). In Leger et al.  
(2025), a perturbed-parameter ensemble of 100 simulations was performed, covering 35-18 ka at 300 m  
206 spatial resolution across the European Alps, an order-of-magnitude improvement over previous 1-2 km  
models (Seguinot et al., 2018; Jouvet et al., 2023). Their model setup (and thus also ours) integrates  
208 modules for ice-enthalpy (after Aschwanden et al., 2012), surface mass balance (after Calov & Greve,  
2005), isostatic adjustment (after Wickert, 2015), and avalanching. The climate forcing was produced by  
210 Russo et al. (2024) (also used by Jouvet et al., 2023), who conducted regional downscaling over Europe  
(2 km resolution) of global Earth-system model outputs using the Weather Research and Forecasting  
212 model, providing gridded fields of temperature and precipitation for both the LGM (24 ka) and the pre-  
industrial era (1850 AD). A glacial index scheme generates continuous climate forcing interpolating these  
214 two states using independent local proxy climate data that combines pollen and speleothem records (Fig.  
2e in Leger et al., 2025; Luetscher et al., 2015; Duprat-Oualid et al., 2017). Basal sliding is parameterized  
216 following a nonlinear Weertman friction condition (e.g. Schoof & Hewitt, 2013) with a sliding coefficient  
also influenced by enthalpy-driven basal meltwater content and elevation-dependent basal materials'  
218 strength, following Bueler & van Pelt (2015) and the Mohr-Coulomb law (Cuffey & Paterson, 2010). For  
the bed topography, as in Leger et al. (2025)'s simulation 37, we use the digital elevation model from Mey  
220 et al. (2016) which includes the removal of (1) present-day glacier thicknesses and lake depths, and (2)  
reconstructed present-day valley-fill sediment thicknesses in main overdeepenings throughout the Alps.  
222 More detailed methods and model descriptions are presented in Leger et al. (2025).



224 Here, we employ this model setup to run two new simulations featuring the additional coupling of 3D  
Lagrangian particle tracking. The first simulation is parameterised for subglacial particle seeding whilst  
226 the second for supraglacial particle seeding (Fig. 1). We run all simulations between 40 and 18 ka, thus  
starting 5 kyr earlier than the original setup. While Leger et al. (2025) showed that starting the simulation  
228 before 35 ka had no noticeable impact on the modelled AIF geometry during the LGM (~24.8 ka in their  
simulations), preliminary tests showed that it does affect the diversity of modelled particle trajectories  
230 (more details in Results section).

## 232 2.2 Particle seeding schemes

234 For each model time step (every 0.01-0.04 yr) and domain cell ( $n = 6,030,036$ ), we implement a set of  
conditions to determine whether to ‘seed’ (i.e. create) a new particle or not. We exclusively focus on  
236 estimating glacial sediment trajectories and transport statistics, and do not address the volumes of glacial  
sediments, erosion, or deposits. Therefore, seeding of a new particle can be interpreted as the creation of  
238 a new glacial ‘sediment entity’ within the glacier system, possibly ranging in size from grains to large  
boulders. Note that throughout this paper, we use the terms ‘glacial sediment’ and ‘glacial transport’ to  
240 describe all sediments that are transported by glacier ice, thus combining supraglacial, englacial, and  
subglacial debris/transport. Below, we describe the set of conditions required for both subglacial seeding  
242 and supraglacial seeding to occur in our model (Fig. 2).

244 The frequency and spatial distribution of subglacial seeding is here set to be a function of basal ice velocity,  
as frequently observed (Humphrey & Raymond, 1994; Herman et al., 2015; Cook et al., 2020; Herman et  
246 al., 2021). Here, we use the subglacial erosion law obtained by Koppes et al. (2015) from results on  
sediment export volumes from several outlet glaciers of the Patagonian and Antarctic Peninsula icefields.  
248 This non-linear erosion law assumes the erosion rate  $\dot{e}$  is proportional to the sliding velocity  $u_s$  raised  
to a power, using an erodibility constant  $K_g = 5.2 \times 10^{-11}$  and a sliding velocity exponent of  $l = 2.34$ :

250

$$\dot{e} = K_g |u_s|^l \quad 1)$$

252

We follow Seguinot & Delaney (2021) and assume glacier systems studied by Koppes et al. (2015) likely  
254 yield similar dynamics to former outlet glaciers of the AIF during the LGM. Using this law, our model  
computes an erosion rate and cumulative erosion over time for each grid cell (Fig. 2). Computed erosion  
256 is not used to modify the bed topography dynamically but rather only as a quantitative proxy for particle  
seeding. Once this artificial cumulative erosion reaches a certain threshold (here set to 4 cm), seeding  
258 occurs and the erosion value is reset to 0, thus adding a new particle to the system (Fig. 2). This value (4  
cm) is arbitrary and represents a parameter to control the total number of advected particles. To add  
260 stochasticity to the modelled creation and freeze-on of subglacial sediment, seeding further requires



meeting a condition of time delay since last seeding occurred. This time delay is set to randomly vary  
262 between 10 and 60 yrs during the simulation following a uniform probability distribution (Fig. 2). Thus,  
even though erosion is positively correlated to basal ice velocity, some randomness is here introduced in  
264 whether seeding will occur shortly or with some delay after the cumulative erosion threshold is reached.  
Note that with this scheme, we do not model the glaciofluvial transport of subglacially eroded materials,  
266 as our model setup is not yet coupled to a subglacial hydrological-routing module. Instead, we exclusively  
focus on subglacially eroded materials which freeze on and are subsequently advected by glacier ice (Alley  
268 et al., 1998). The limitations of this assumption are further mentioned in the Discussion section.

270 For supraglacial seeding, our scheme was conceived to simulate mechanisms generating supraglacial  
debris on glaciers, i.e. gravitational mass wasting events including rockfall, rock avalanches, debris flow,  
272 avalanches, or landslides (Benn et al., 2012). We assume these events require both no (or little) ice cover  
and steep slopes to occur. We define all slopes steeper than  $45^\circ$  as susceptible to mass wasting (Fig. 2),  
274 following recommendations from Fischer et al. (2012). However, our 300 m model resolution still smooths  
high-elevation peaks and steep slopes resulting in fewer locations  $>45^\circ$  steep than in reality. To avoid this  
276 bias, we use a higher-resolution digital elevation model (30 m resolution; Tadono et al., 2014) to produce  
a mask of pixels meeting a  $>45^\circ$  slope condition. We consider all modelled ice that is  $<20$  m thick and  
278 located in pixels meeting the high-resolution  $>45^\circ$  slope mask to be an artifact of our 300 m resolution,  
thus representing regions that would have no (or negligible) ice cover in reality. As a result, in our setup,  
280 a given grid cell needs to both satisfy the  $>45^\circ$  slope condition (in the high-resolution mask) and display  
modelled ice thickness  $<20$  m, for supraglacial seeding to occur (Fig. 2).

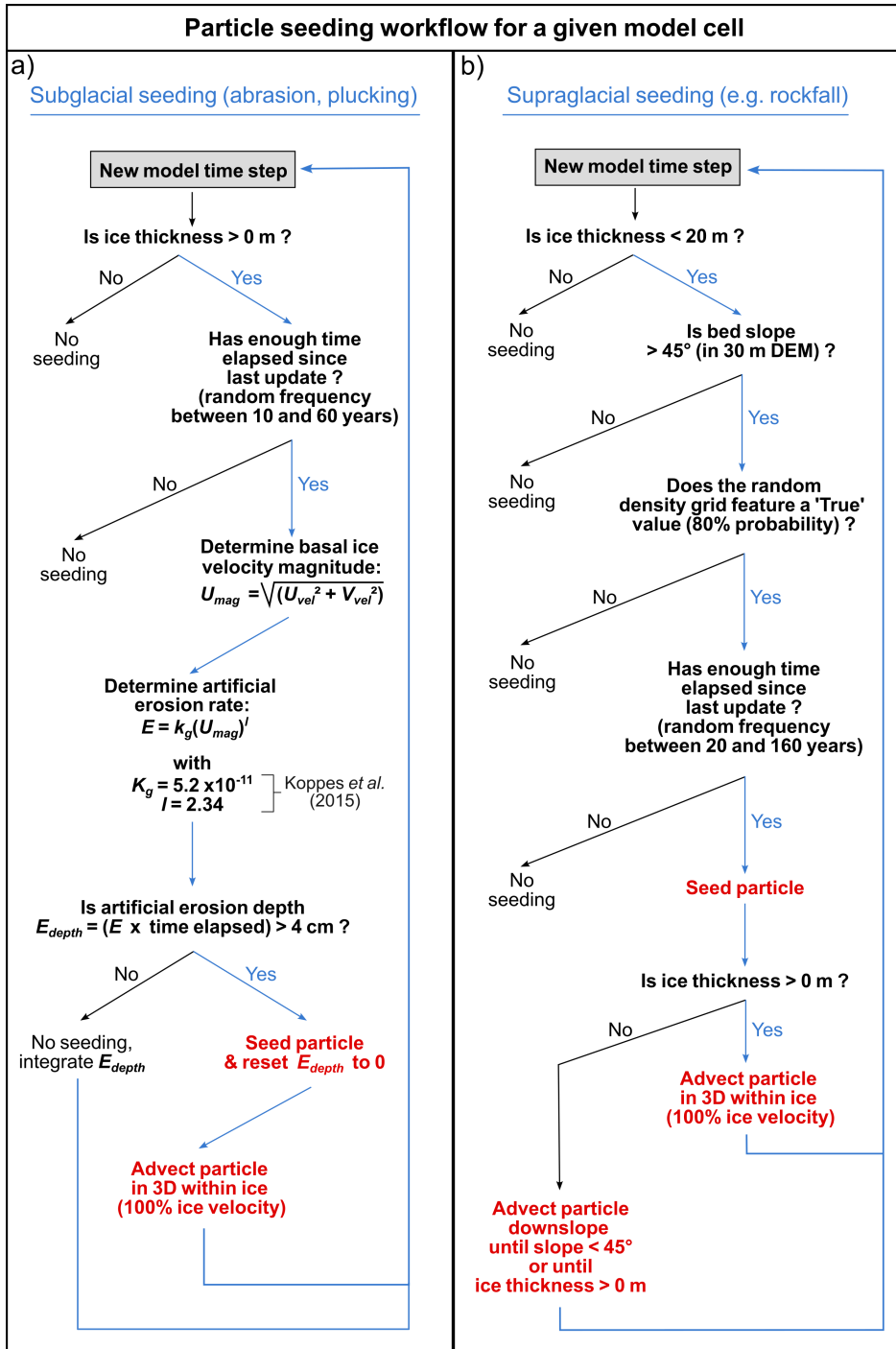
282

As with subglacial seeding (see above), we introduce stochasticity in supraglacial debris production.  
284 Firstly, supraglacial seeding only occurs when meeting a Boolean mask condition (True/False array)  
randomly shuffled for all domain cells (at every time step) with a True-value likelihood of 80%. Following  
286 this, seeding also only occurs when meeting a time delay set to randomly vary between 20 and 160 yrs  
during the simulation (Fig. 2). All random sampling follows a uniform probability distribution. These  
288 additional conditions separately add temporal and spatial randomness to supraglacial seeding, thus  
applying a probabilistic algorithm; common in mass-wasting event modelling (e.g. Champel et al., 2002).  
290 Therefore, while gravitational mass wasting events are highly likely where/when the model features steep  
slopes ( $>45^\circ$ ) and a lack of ice cover, they are not necessarily going to occur at every time step and always  
292 in the same locations (Fig. 2). Once seeded, particles are advected downslope following the steepest  
descent until slope angle  $<45^\circ$ , or until reaching cells with modelled ice, in which case ice advection will  
294 take over (Fig. 2).

296



298  
300  
302  
304  
306  
308  
310  
312  
314  
316  
318  
320  
322  
324  
326  
328  
330  
332  
334  
336



338 **Figure 2.** Decision chart indicating the model workflow specific to our particle seeding schemes for a given  
 340 model cell ( $n = 6,030,036$ ), and for the two cases of (a) subglacial seeding (abrasion, plucking) and (b)  
 342 supraglacial seeding (e.g. rockfall, rock avalanche, debris flow, landslides, etc.). This chart summarizes the  
 set of conditions and parameters applied to every model cell and at every model timestep (every 0.01-0.04 yr)  
 during the simulation in order to seed, or not seed, a new particle within the model system.



344

### 2.3 Particle Lagrangian advection scheme

346

To track the movement of particles in 3D within the evolving glacier geometry, we use a Lagrangian advection scheme which computes the space-time trajectory of particles created from seeding and resolves the precise 3D positions of particles at sub-grid resolution. At each model timestep, IGM computes the 3D ice-flow based on a high-order stress-balance model referred to as the ‘Blatter-Pattyn’ model (Blatter, 1995) and thus outputs a 3D velocity field. Each particle’s horizontal ( $x, y$ ) and vertical ( $z$ ) positions are thus updated according to ice velocity components  $u, v, w$ , respectively, integrated over a model timestep,  $\Delta t$ , using an explicit Euler scheme.

$$\begin{aligned}x^{n+1} &= x^n + \Delta t \cdot \bar{u}, \\y^{n+1} &= y^n + \Delta t \cdot \bar{v}, \\z^{n+1} &= z^n + \Delta t \cdot \bar{w},\end{aligned}\tag{2}$$

where  $\bar{u}, \bar{v}, \bar{w}$  represent the bilinearly interpolated horizontal and vertical velocities, respectively, at a particle’s current location ( $x^n, y^n$ ). We ensure no particles artificially leave the ice column due to numerical integration errors or transient velocity fluctuations by clipping their relative (normalized) vertical positions to between 0 (bed) and 1 (ice surface). The bilinear interpolation for a scalar field  $f$  at a sub-grid location ( $x, y$ ) is computed using:

$$\bar{f}(x, y) = \sum_{i,j} f_{i,j} \cdot (1 - |x - i|) \cdot (1 - |y - j|)\tag{3}$$

where the summation runs over the four grid nodes surrounding the particle’s horizontal position, and the weights  $(1 - |x - i|)$  and  $(1 - |y - j|)$  ensure a smooth linear interpolation based on the distances to these nodes.

We assume all particles are advected at the velocity of the ice. The limitations of this assumption are assessed in the Discussion section below. When a particle reaches the modelled ice margin and is deposited, i.e. when ice thickness at its position becomes 0 m, it is prescribed the bed elevation. If local slope is  $<45^\circ$  this particle will remain stagnant (Fig. 2). If the modelled glacier re-advances and local ice thickness is  $>0$  m again, the particle gets re-entrained and 3D ice advection computations restart. We thus assume that all temporarily deposited sediments freeze-on and get re-entrained by a re-advancing ice margin. Although reality is more complex whereby former deposits can be overridden and survive younger glacier advances, the process of re-entrainment is here considered to dominate (Cogez et al., 2018). This assumption is supported by the general rarity, in formerly glaciated landscapes, of preserved older moraines inboard of younger and more extensive terminal moraines (Gibbons et al., 1984).



380

Although particle positions are computed at every timestep (0.01-0.04 yr), they are saved every 10 model  
382 years, which for our simulated timeframe (40-18 ka) generates 2200 data frames for each of the millions  
of advected particles (20.5 million at maximum). The data saved for each particle include its  $x$  and  $y$   
384 coordinates, relative height in ice column, seeding year, and cumulative glacial transport time since  
seeding. 10 years is the highest output frequency achieved while ensuring the particle database (~1.22 TB)  
386 can be post-processed at a manageable computational cost. At that output temporal frequency, the post-  
processing mapping of particle trajectories fully reflects the simulated ice-flow and particle advection in  
388 most cases, except where modelled ice velocities are both high (e.g.  $>1000 \text{ m yr}^{-1}$ ) and towards highly  
sinuous glacier motion (e.g. around valley bends), where mapping particle positions every 10 years can  
390 result in unrealistically straight trajectories. This will however only impact the mapped trajectory towards  
the bend and not reduce the accuracy of its modelled provenance nor destination.

392

#### 2.4 Reconstructing glacial sediment trajectories

394

After running the glacier-particle coupled IGM simulations, we use the output database of particle  
396 coordinates to map the time-transient trajectories of certain particles. This is conducted within the frame  
of two analyses. The first one, hereafter referred to as the ‘sink-to-source’ analysis, aims at reconstructing  
398 the provenance and glacial transport pathways of specific LGM terminal ice-contact deposits. The second  
analysis, called ‘source-to-sink’, addresses the opposite question. Its objective is to estimate the possible  
400 transport pathways and deposition locations of glacial sediments eroded from a pre-determined source.

402 The sink-to-source analysis consists in finding all particles that end up within the area of a mapped deposit  
at the end of the simulation (18 ka), after final glacier retreat, and trace back their glacial transport  
404 trajectories. Although this can be achieved for any user-defined polygon, we focus on ice-contact deposits  
located towards the terminal margins of main AIF outlet glaciers during the LGM (e.g. LGM moraines).  
406 To follow a consistent methodology across the Alps, we map a series of 49 polygons (Fig. 3a) covering  
the area between our most extensive time-independent modelled ice margin and the empirical LGM outline  
408 of the AIF originally produced by Ehlers et al. (2011) and improved by several studies since (Gianotti et  
al., 2008; 2015; Ravazzi et al., 2012; Monegato et al., 2017; Federici et al., 2017; Ivy-Ochs et al., 2018;  
410 Braakhekke et al., 2020; Kamleitner et al., 2022; 2023; Ribolini et al., 2022). Tracing polygons over that  
area between ensures to isolate all particles deposited at the LGM margins even where model-data fit in  
412 ice extent is not perfect, which is still the case despite improvements relative to former AIF-wide LGM  
models (Seguinot et al., 2018; Jouvet et al., 2023; see Fig. 4a in Leger et al., 2025).

414

416



418  
420  
422  
424  
426  
428  
430  
432  
434  
436  
438  
440  
442  
444  
446  
448

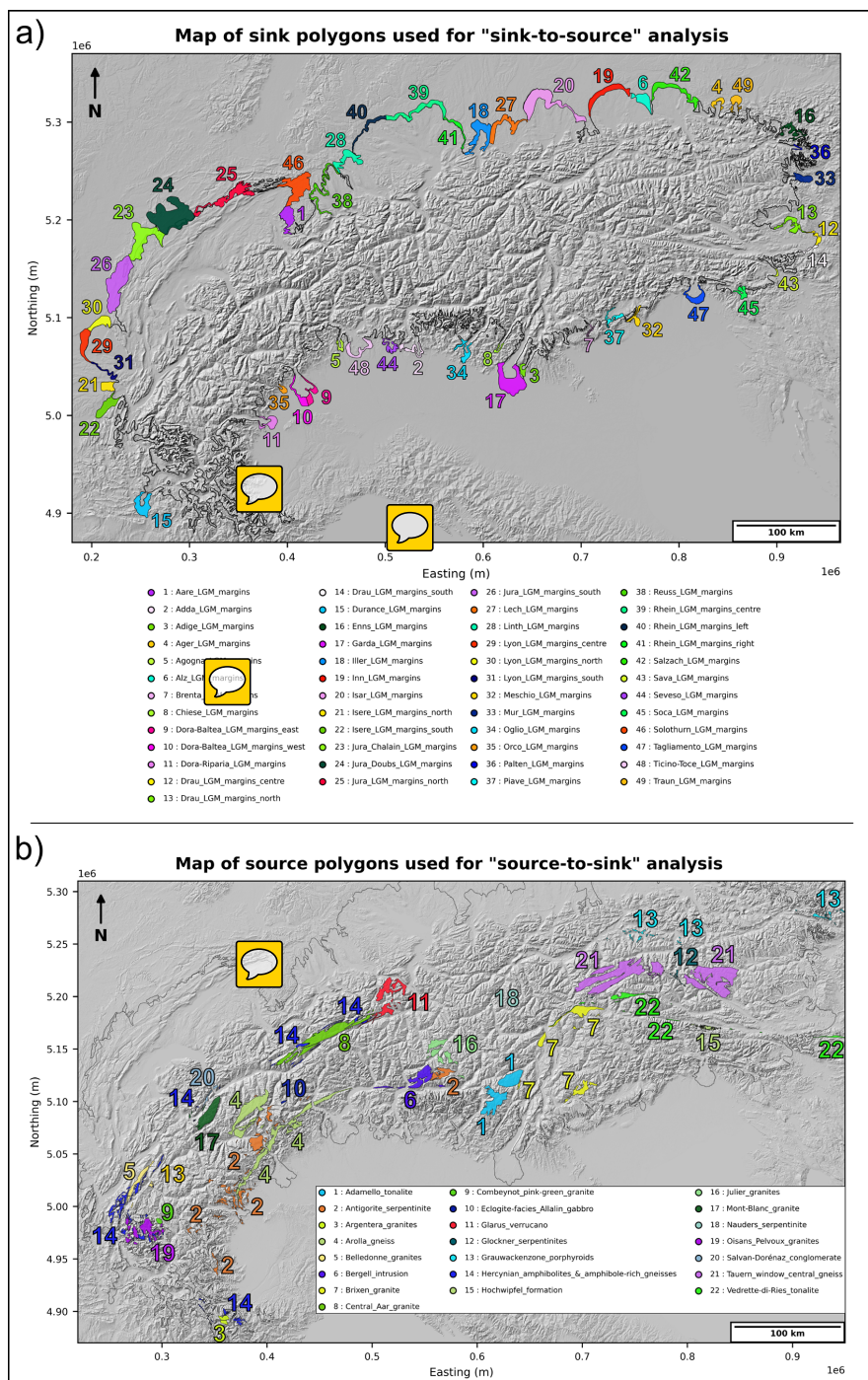


**Figure 3.** Maps of all sink and source polygons used for producing both catalogues of (a) sink-to-source and (b) source-to-sink analyses and their resulting particle trajectories. Sink polygons (a; n = 49) were selected and mapped to represent terminal ice-contact deposits for all major outlet glaciers of the Alpine Ice Field (AIF) during the Last Glacial Maximum (LGM) while source polygons (b; n = 22) were selected and mapped from geological data on surface outcrops for key lithologies across the Alps (more details in section 2.4). In this and all subsequent paper figures displaying geo-spatial data, X and Y coordinates are displayed as projected (unit: m) in the WGS 84 / UTM zone 32N (EPSG:32632) coordinate reference system.



456

Importantly, our 49 sink polygons (Fig. 3a) are not a precise map of terminal LGM ice-contact deposits preserved in the Alps. However, they are useful to produce a first-order estimation of possible LGM glacial trajectories for deposits located towards major outlet glacier margins, pre-erosion. Producing an Alps-wide, digital and open-access map of all preserved terminal ice-contact deposits dating to the LGM (e.g. Clark et al., 2018; Davies et al., 2020) has yet to be achieved in the Alps and is beyond the scope of this study. To estimate the relative contributions of various provenances to the total particle number found in a sink deposit, we divide our Alps-wide domain in 241 present-day hydrological catchments; obtained from the global HydroBASINS database (Lehner & Grill, 2013), and named based on catchment-specific river names (Figure S1). Our sink-to-source analysis produces a catalogue of modelled particle trajectories, estimated provenance fractions per basin, and statistics including glacial transport time and particle age (i.e. seeding year), for all particles found in each of the 49 sink polygons shown in Figure 3a. All results are produced separately for subglacial and supraglacial particle seeding, enabling us to compare the impacts of different sourcing mechanisms on glacial sediment transport histories and provenances.

470

For the source-to-sink analysis, we select sources that represent mapped outcrops of specific alpine surface lithologies, to estimate the glacial transport pathways of sediments from specific rock types between 40 and 18 ka, across the Alps. We focus on rock type as this enables us to compare modelled estimates against empirical data on ice-contact deposits (e.g. erratic boulders) of known lithologies and locations post-retreat (e.g. Braakhekke et al., 2020; Monegato et al., 2022). This requires identifying surface lithologies specific enough to be associated with mapped outcrops and uniquely recognisable through geological assessment of ice-contact deposits. The outcrops moreover need to cover a large-enough area for enough particle seeding to overlap them, given that a single grid cell is 90,000 m<sup>2</sup>. To identify such lithologies, we use the open-access 1:500,000-scale geological map sheets 1 and 2 from the ‘Structural model of Italy’ (Bigi et al., 1990a; b). These maps present a relatively high spatial resolution, are easily accessible online and georeference-able, and provide a consistent naming convention of lithologies across the entire Alps. We also use geodata derived from the Geological Map of Austria 1:50.000 sheets 197 Kötschach and 198 Weißbriach for one extra lithology (i.e. the Hochwipfel formation) (Geologische Bundesanstalt Österreich, 2021a, b). We then isolate a subset of 22 surface lithologies referred to as our ‘source polygons’ (Fig. 3b). While these are not a comprehensive list satisfying the above criteria, they are spatially widespread and cover the main rock types described by investigations on LGM erratic boulders in the Alps. They include Mont-Blanc granite (Bussien Grosjean et al., 2018), Glarus Verrucano (Letsch et al., 2015), or Salvan-Dorénaz conglomerate (Capuzzo et al., 2003), for instance (Fig. 3b).

The source-to-sink analysis consists in finding all particles seeded within our 22 source polygons during the AIF simulations, and in mapping their glacial transport pathways. Due to existing mechanisms of sediment melt-out and lodgement at the ice-bed interface (Alley et al., 1997), we consider any location



along the resulting trajectories to be a possible destination for glacial sediment of the studied lithology.  
494 Thus, the source-to-sink analysis produces a catalogue of maps displaying modelled trajectories of  
particles seeded within each of the 22 selected surface lithologies shown in Figure 3b. The maps are  
496 produced for both subglacial and supraglacial particle seeding allowing for a direct comparison between  
the two.

498

Consequently, the main outputs of this study are the ‘sink-to-source’ and ‘source-to-sink’ analyses, i.e.  
500 two catalogues of model results shared under the form of maps displaying source and sink particle  
trajectories, pie charts of deposit provenance fractions, histograms showing data from sink particles, and  
502 polyline shapefile data for visualization in GIS softwares. These data are all accessible from the Zenodo  
repository attached to this paper (link: <https://doi.org/10.5281/zenodo.18374156>).

504

## 506 **3 Results**

### 508 **3.1 GPUs reduce the computational cost of particle tracking**

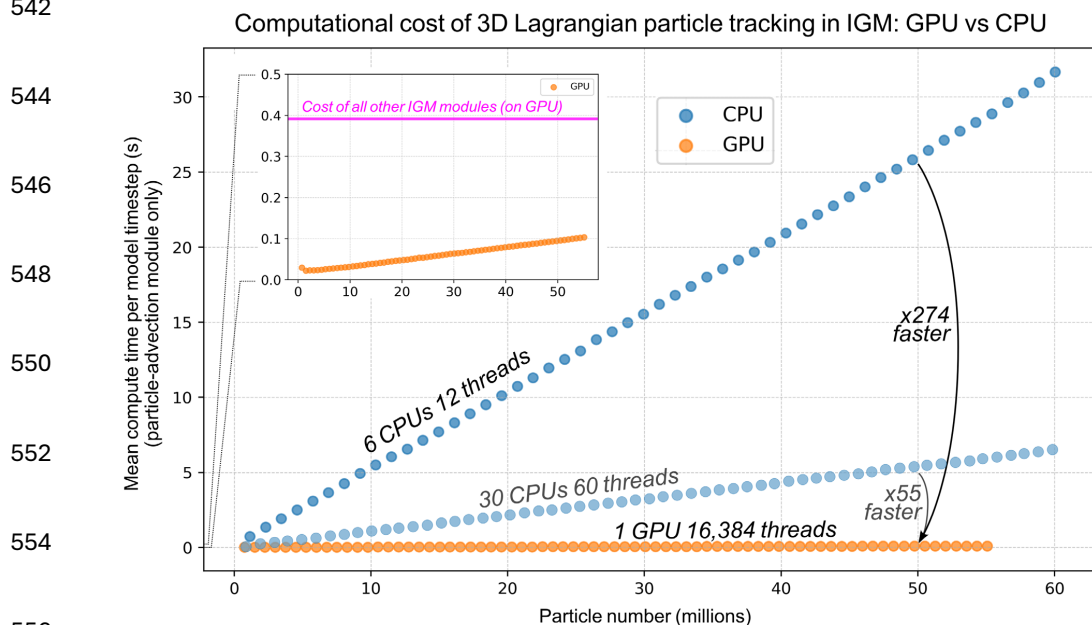
510 GPUs are particularly well-suited for particle-based numerical modelling, such as Lagrangian particle  
tracking, due to their architecture optimized for massively parallel execution of small, independent  
512 computations, ideal for processing individual particles concurrently. This contrasts with traditional  
computing on Central Processing Units (CPU) which restricts the parallelization of such small operations  
514 on much fewer cores. Consequently, GPU-accelerated algorithms for particle-based modelling have been  
extensively developed in fields as varied as fluid mechanics, graphics, or geosciences (e.g. Wang et al.,  
516 2022; Aaron, 2023). In our specific application, we find that transferring all computation on the GPU  
makes 3D Lagrangian particle advection highly efficient, with a computational cost that remains small  
518 even when tracking tens of millions of particles within a modelled glacier (Fig. 4).

520 To quantify this gain, we ran a test simulation over the majority of the European Alps and, after initializing  
an LGM Alpine Ice Field (AIF), seeded new particles in all grid cells of the glacier accumulation area  
522 every two model years, thus quickly multiplying the total particle number. When operating on a single  
GPU (Nvidia RTX 4090), raising the number of particles from 0 to 50 million increases the mean cost of  
524 computing their advection linearly between 0.02 and 0.1 seconds per timestep (Fig. 4). Even with 50  
million particles in the system, the computational cost of particle tracking remains below 26% of the mean  
526 cost (i.e. ~0.39 seconds per timestep) of all other IGM processes and modules in our Alps-wide simulation  
of the LGM at 300 m resolution. When running the same test using multiple CPUs instead, the mean costs  
528 of tracking 50 million particles reach approximately 26 and 5.5 seconds per timestep using 12 and 60 CPU  
threads, respectively (Fig. 4). These computational costs are between 274 and 55 times greater than those



530 obtained with a single GPU, respectively. For 10 million advected particles, the costs are still 200 and 42  
times greater than with the GPU, respectively. This shows that when using any traditional CPU-based  
532 glacier evolution model, coupling Lagrangian tracking of large particle numbers ( $>10^7$ ) would  
substantially increase the simulation's computational cost. The alternative of accurately computing  
534 particle trajectories using post-processing only (after simulations are run), although not computationally  
restrictive, would be made impossible by the data volume of transient 3D velocity fields that would need  
536 to be saved at every time step (0.01-0.04 yr), which in our case would quickly exceed the hundreds of  
Terabytes. Contrastingly, when using IGM and a GPU-based approach, 3D particle tracking of large  
538 particle numbers can be coupled to simulations with only a small additional cost relative to the ice-flow  
model (Fig. 4). This enables us to run, for the first time, IGM simulations at high (300 m) spatial  
540 resolutions with millions of particles tracked over Alps-wide and multi-millennial scales, an experiment  
that would be unfeasible using traditional CPU-based computing.

542



558 **Figure 4. Mean computational time/cost (in seconds) of computing the Lagrangian 3D advection of particles**  
in ice during a single model timestep of our Alpine-Ice-Field simulations with the Instructed Glacier Model  
(IGM), as a function of particle number. The data shown here allows one to compare the computational  
560 cost of Lagrangian particle tracking on a single GPU (orange dots; Nvidia RTX 4090) relative to computing it on  
multiple CPU cores (blue dots; Intel(R) Xeon(R) CPU E5-2620 v3). The difference between blue and orange  
562 dotted lines highlights the significant computational gain of parallelizing particle advection operations on the  
GPU. The intermediate line of blue dots (30 CPUs, 60 threads) is shown with slight transparency as numbers  
564 were calculated assuming linear proportionality to the real computational costs obtained with a 6 CPU (12  
threads) setup. The inset graph changes the Y scale and zooms inside compute time values  $<0.5$  seconds,  
566 allowing one to visualize the linear increase in cost with increasing numbers of advected particles when using  
the single GPU (otherwise invisible). The inset also compares this particle-module cost against the average  
568 computational cost ( $\sim 0.39$  s; pink line) of a single model timestep when combining all other GPU-based IGM  
modules used when running the Alps-wide 300 m best-fit simulation of Leger et al. (2025): i.e. the same  
570 simulation we re-run in this study.



572

### 3.2 Alps-wide patterns of glacial sediment sourcing

574

Our coupled glacier-particle simulations output a database of 3D particle coordinates and other statistics from the moment of seeding until the end of the glacier simulation (i.e. 18 ka). Thus, for both simulations with subglacial and supraglacial particle seeding, a map of seeding locations for each of the ~20.5 million advected particles can be produced. To visualize the spatial heterogeneity of particle seeding, we transform the seeding location data into normalized seeding density maps (Fig. 5). In Figure 5, bright colours (normalized density closer to 1) show regions with relatively more particle seeding events during the simulations. For subglacial seeding, these regions are associated with high basal ice velocities modelled during extended periods of the simulation, spanning 40-18 ka. These can be interpreted as likely to produce the largest volumes of glacial sediments of subglacial origin (e.g. abrasion and plucking) during the LGM. Potent subglacial sediment sourcing regions include the Rhône valley between Montreux and Sion (Switzerland), the Dora Baltea valley between Aosta and Ivrea (Italy), the Romanche valley between Le Bourg-d'Oisans and Grenoble (France), or the Rhein valley between Domat/Ems (Switzerland) and Bregenz (Austria), for instance (Fig. 5a).

588

For supraglacial seeding, regions of high seeding densities are those presenting steep topographies ( $>45^\circ$ ) and ice-free conditions (or thin ice covers:  $<20$  m) during extended time-periods of the simulation. These regions also need to be near dynamic modelled glaciers for seeded particles to eventually get transported by glacier ice. These regions are interpreted as likely to have produced the largest volumes of supraglacial sediments (e.g. from rockfall, debris flow, landslides, avalanches) during the LGM. Our results suggest that high supraglacial sediment sourcing regions are widespread (Fig. 5b) but include, for instance, the Écrins Massif (France), the Lepontine Alps (Switzerland), the Dolomiti Bellunesi Massif (Italy), the Triglav Massif (Slovenia), or the Bernese Alps (Switzerland). During the LGM, these regions are most concentrated within a narrow band located towards the northern and southern peripheries of the alpine arc, where high topographies ( $> 2500$  m a.s.l.) combined with thin/no ice cover maximize the likelihood of nunatak occurrence (Fig. 5b). Contrastingly, supraglacial sediment sourcing is lower further towards the Alps' interior, where the model produces greater ice thicknesses and topographic ice covers for extended periods, thus reducing nunatak occurrence.

602

604

606



608

610

612

614

616

618

620

622

624

626

628

630

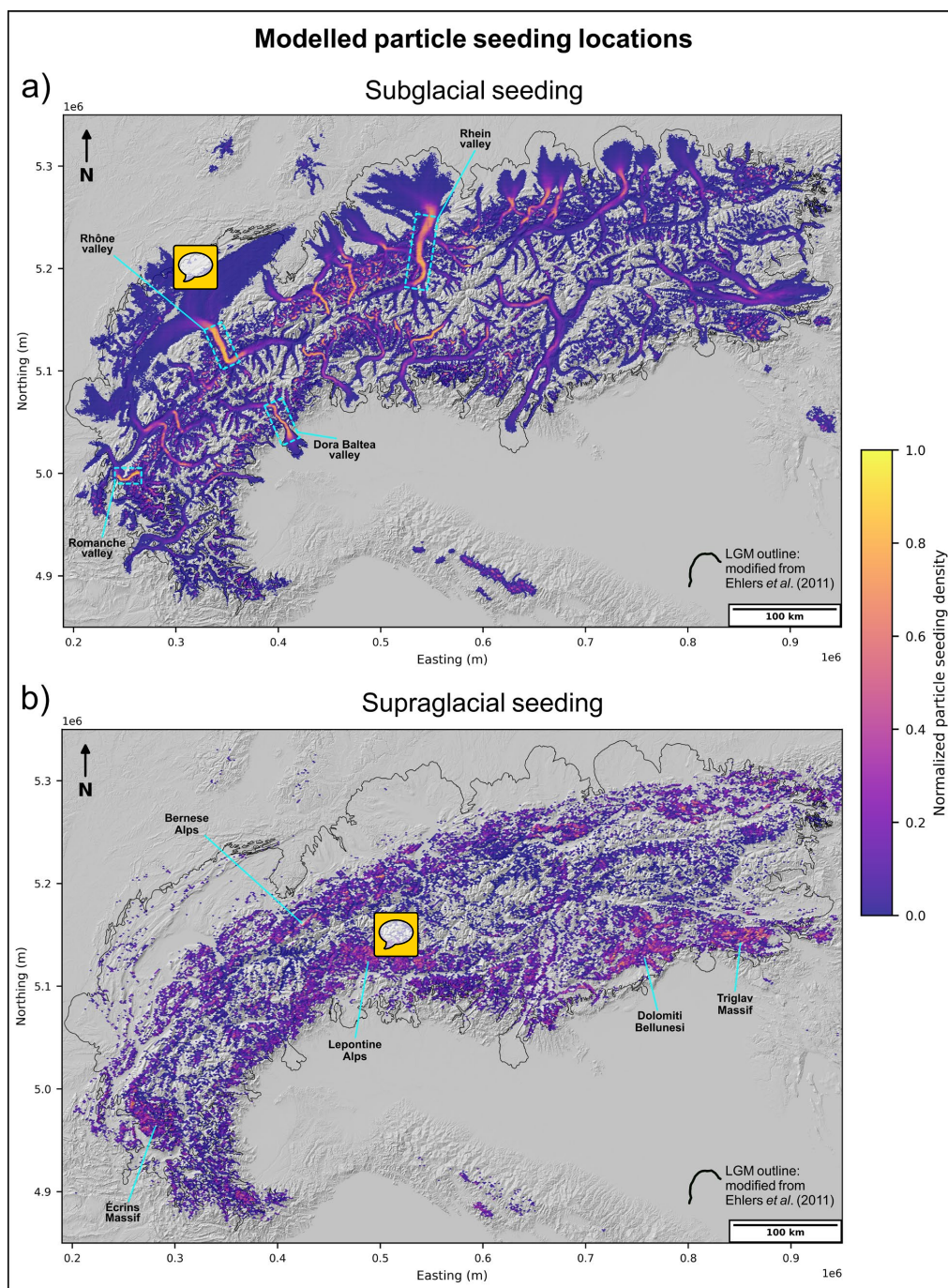
632

634

636

638

640



642

644

646

648

**Figure 5. Maps showing the seeding locations of all modelled particles (~20.5 million at maximum) in both simulations with (a) subglacial and (b) supraglacial particle seeding. The maps are divided into small hexagons in which the total number of seeded particles is computed. Hexagons are colored based on this total number normalized across the entire dataset, resulting in a density map of particle seeding locations, with brighter yellow colors indicating relatively more seeding, and darker purple colors indicating relatively less seeding. A lack of colors (grey hillshade background) indicates no particle seeding occurred at any time during simulations.**




### 650 3.3 The sink-to-source analysis and catalogue

652 With the sink-to-source analysis, we produce a catalogue of modelled time-transient trajectories for  
terminal LGM ice-contact deposits mapped across the Alps, hereafter referred to as our ‘sinks’ (see section  
654 2.4). Sink-to-source trajectories reveal the modelled pathways of ice-advected particles ending up within  
these sinks after final glacier retreat. For each sink polygon mapped ( $n = 49$ ; Fig. 3a), we provide a high-  
656 resolution map of particle trajectories, along with an estimation of particle provenance fractions. For each  
sink and particle in this sink, we also produce statistics on total particle glacial transport distance,  
658 cumulative glacial transport time, cumulative time in ice-free conditions during source-to-sink journey,  
and seeding year (i.e. timing of erosion). These data are produced for both cases of subglacial and  
660 supraglacial seeding, enabling us to quantify differences in glacial transport dynamics between the two.  
We consider the sink-to-source catalogue to be a main result of this study and encourage readers to  
662 download it from the Zenodo repository attached to this paper (link:  
<https://doi.org/10.5281/zenodo.18374156>). All particle trajectory data for each seeding type and sink are  
664 also available as polyline shapefiles for visualization in GIS software.

#### 666 3.3.1 A sink-to-source case study: the Inn glacier LGM margins

668 As a case study, we here describe the results of our sink-to-source analysis for a single ice-contact deposit,  
i.e. the Inn glacier LGM margins (sink 19; Fig. 6). We chose this outlet glacier as its modelled ice-flow  
670 during the LGM originates from a large variety of catchments, produces numerous transfluences, has been  
the subject of several studies (e.g. Reitner, 2007; van Husen, 1997), and produces a good ice-extent fit  
672 during maximum expansion with empirical data (see Fig. 1a in Leger et al., 2025). In our subglacial and  
supraglacial seeding simulations, totals of 53,797 and 36,945 particles end up within this ice-contact  
674 deposit, respectively (Fig. 6). The sink particles originate from 15 (for subglacial seeding) and 12 (for  
supraglacial seeding) different hydrological basins. Our modelling suggests the basin contributing the  
676 most ice-contact sediments of subglacial origin is the Inn-Simsee basin (basin 44; Figure S1), with an  
estimated provenance fraction of 42.5% (Fig. 6). For supraglacial seeding, the distribution of provenance  
678 fractions is different. The basin estimated to provide the most sediments of supraglacial origin is the Ziller  
basin (basin 191; Figure S1), although its provenance fraction (32%) is tied with the Alz-Traun basin  
680 (basin 63, 29.5%). On average, our modelling suggests that ice-contact deposits of the LGM Inn glacier  
margins spent  $3,021 \pm 4,114$  yrs (median  $\pm$  interquartile range) in glacier ice for those of subglacial origin.  
682 This median number is approximately twice greater for ice-contact deposits of supraglacial origin, with a  
cumulative glacial transport time of  $6,361 \pm 3,641$  yrs (see section 3.3.2 for why). At maximum, particles  
684 are modelled to spend up to 12,644 and 14,613 yrs in ice for subglacial and supraglacial seeding,  
respectively (Fig. 6e, f). Particles yielding such high glacial transport times are few ( $<300$ ) and frequency



686 distributions tail off, which indicates that starting our simulations at least 15 kyr before the local LGM  
688 (~24.8 ka) is both important and adequate (Fig. 6e, f). On average, ice-contact deposits of the Inn LGM  
690 margins are modelled to have travelled over  $78 \pm 80$    $138 \pm 81$  km for sediments of subglacial and  
supraglacial origin, respectively. Ice-contact deposits of subglacial origin are estimated to have spent, on  
692 average, a total of  $353 \pm 1936$  yrs in ice-free conditions during their source-to-sink journey. This time in  
ice-free conditions occurs when particles are deposited following temporary ice retreat, prior to re-  
694 entrainment by subsequent advances (see videos in supplement). This median number increases fivefold  
to  $1885 \pm 3719$  yrs for sediments of supraglacial origin, suggesting a greater potential for atmospheric  
696 exposure during their transport (assuming they remain at the Earth's surface). In line with these  
estimations, the results suggest that ice-contact deposits of the Inn LGM margins and of supraglacial origin  
are on average eroded 5090 yrs earlier than those of subglacial origin (Fig. 6).

698 For these Inn glacier LGM margin deposits, the modelled trajectories of subglacially-seeded sediments  
display similar pathways than those of supraglacial origin. However, we find that glacial sediments of  
700 supraglacial origin, due to reaching glacier surfaces from nunataks and valley/glacier sides, are more likely  
to produce trajectories resembling well-defined medial moraines (e.g. Fig. 6b, basins 170, 150). We find  
702 this is rarely the case for modelled trajectories of subglacially-seeded particles, which can originate from  
across the glacier bed, including from valley/glacier centres where basal velocities are highest. This  
704 difference also explains why subglacially seeded particles spread over the entire terminal perimeter of the  
Inn glacier's piedmont lobe during the LGM. However, particles of supraglacial origin rarely reach the  
706 glacier's centreline and are pushed sideways by flow divergence within the piedmont lobe, causing  
preferential advection to both the left and right lateral margins of the terminal lobe, but not to its centre  
708 (Fig. 6). We observe a similar trajectory differentiation between ice-contact deposits of subglacial versus  
supraglacial origin for the Garda (sink 17) and the Ticino-Toce (sink 48) outlet glaciers, towards their  
710 modelled piedmont lobes (see 'sink-to-source' catalogue). This mechanism has important implications for  
sampling frontal moraines for detrital thermochronology and linking sampling locations to catchment  
712 provenances (e.g. Bernard et al., 2020).

714 These results focus on a single LGM ice-contact deposit, or 'sink', as an example. The same data were  
obtained for all 49 mapped sinks (Fig. 3a) and can be viewed via the sink-to-source analysis catalogue  
716 (link: <https://doi.org/10.5281/zenodo.18374156>).

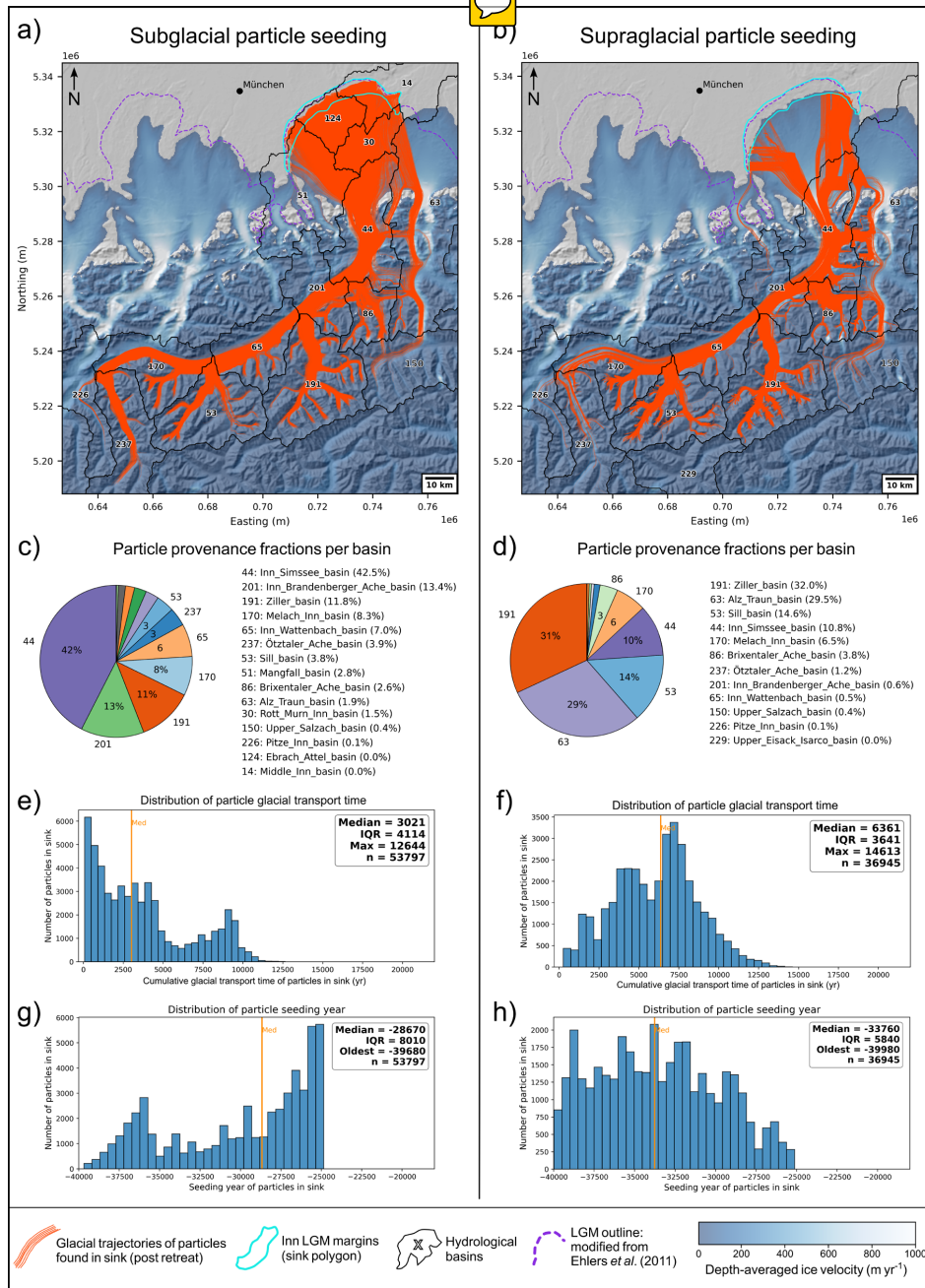
718

720

722



724  
726  
728  
730  
732  
734  
736  
738  
740  
742  
744  
746  
748  
750



752

**Figure 6.** Sink-to-source analysis and resulting modelled particle trajectories (a, b) and transport statistics (c-h) for subglacially (a, c, e, g) and supraglacially (b, d, f, h) seeded particles ending up in the chosen sink (cyan polygon) following final glacier retreat. Here, results are shown for a single example sink (or ice-contact deposit) from our sink-to-source catalogue (n=49 sinks in total), i.e. the Inn glacier LGM margins (sink 19: see Fig. 3a for location). The pie charts (c, d) and associated legends indicate the provenance fractions of all particles ending up in this sink for each hydrological basin (mapped and numbered in black on panels a, b) in which they were seeded (see Figure S1). Histograms (e-h) display the resulting distributions of sink particle cumulative glacial transport times and seeding years (i.e. particle age). ‘IQR’ stands for ‘Interquartile Range’: i.e. the spread of middle 50% of the dataset: 75<sup>th</sup> – 25<sup>th</sup> percentiles.

754  
756  
758  
760



762

### 3.3.2 Ice-contact deposits of subglacial versus supraglacial origin

764

As described above for Inn glacier LGM deposits, we find notable differences in glacial transport histories and characteristics between ice-contact deposits of subglacial versus supraglacial origin. Similar differences hold true when analysing all 49 sinks and the 3.1 million particles deposited within them (Fig. 7). For the majority of these sinks (41 out of 49), cumulative glacial transport time is on average greater for particles of supraglacial origin. When averaging over all sinks, the particle glacial transport time is higher by approximately 1925 years, i.e. a factor of 1.9 increase. The total ice-free time (pre-deposition) of sink particles during their source-to-sink journey is also higher for those of supraglacial origin in 41 out of 49 cases, and on average by 1519 yrs, a factor of  $\sim 2.74$  increase (Fig. 7). We find a similar pattern for the age (i.e. the seeding year) of sink particles, which is older (on average by 4640 yrs) for those of supraglacial origin in 46 out of 49 cases. Thus, our modelling suggests that in the Alps, LGM terminal ice-contact deposits of supraglacial origin were likely to be eroded earlier in time, spend more time in or on glacier ice, and spend more time exposed in ice-free conditions during their full source-to-sink journey (Fig. 7). This is likely caused by glacial sediment of supraglacial origin reaching the glacier surface mainly in accumulation areas, where steep topographies protrude, and where ice velocities are lower.

Unlike subglacially-eroded materials which are preferentially produced in fast-flowing areas often located closer to terminal deposits, supraglacial debris requires (on average) more time to be advected to lower glacier elevations and areas of faster-flowing ice and, in turn, to the terminus. Moreover, glacial sediments of supraglacial origin tend to reach contact with ice towards slope-adjacent glacier sides, making them likely to remain near lateral ice margins during glacial transport. This increases their chances of deposition during temporary periods of ice retreat and thinning, which can increase their cumulative ice-free time during their source-to-sink journey. In contrast, subglacially-eroded sediments will preferentially be concentrated towards the faster-flowing centreline of glaciers, further away from lateral glacier margins. These results have implications for terrestrial cosmogenic nuclide exposure dating of moraine sediments deposited by alpine glaciers and other topographically constrained icefields (Heyman et al., 2011). Indeed, they imply that ice-contact deposits of supraglacial origin are more likely to yield cosmogenic nuclide inheritance signals relative to those of subglacial origin, not only because of pre-transport exposure, but also due to potentially longer and more complex glacial transport histories. However, one must note that clast erosion during glacial transport can counterbalance this mechanism and instead remove nuclide inheritance signals (Matthews et al., 2017) (more details in Discussion).

796

798

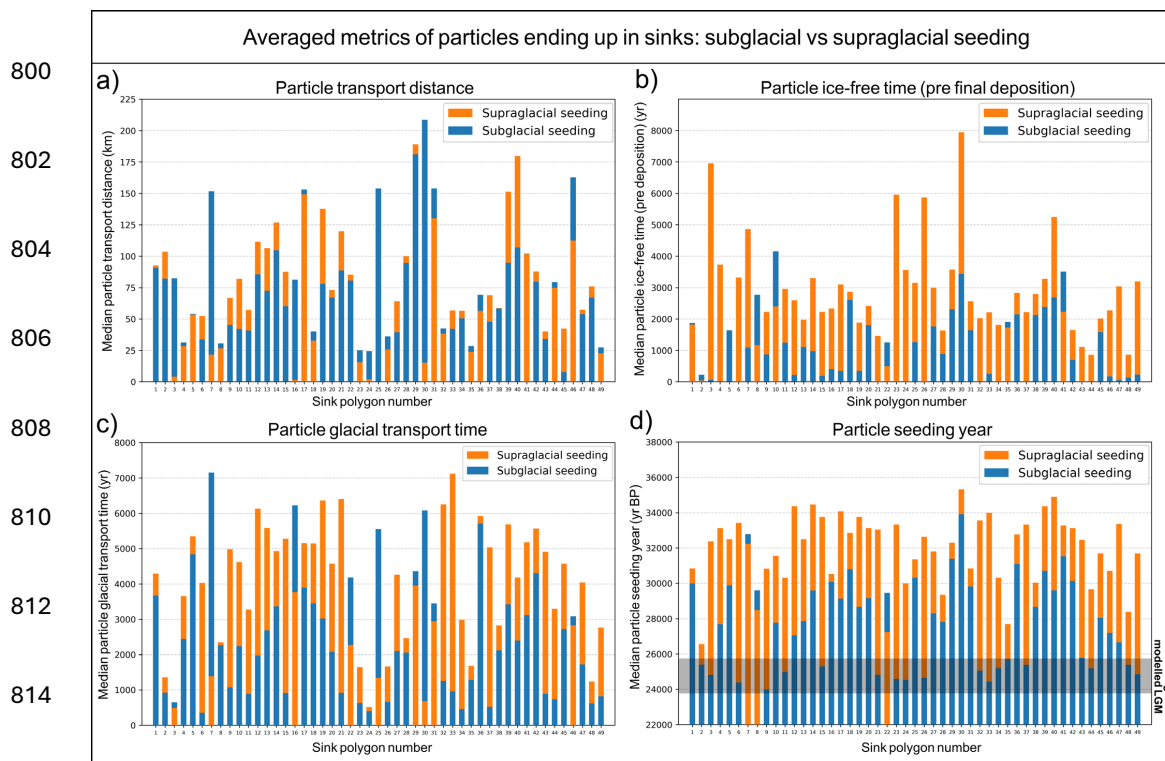


**Figure 7.** Overlapping bar plots (non-stacked) indicating particle statistics averaged over all sink particles (median) for each of the 49 sinks (or ice-contact deposits) in our catalogue (x axis), shown separately for both subglacial seeding (blue bars) and supraglacial seeding (orange bars). See Fig. 3a (or catalogue) to visualize the locations and names of these 49 sinks. The data are shown for four distinct particle metrics, i.e. the median sink particle transport distance (a), the median cumulative time a particle spent in ice-free conditions during its full source-to-sink journey (b), the median cumulative particle glacial transport time (c), and the median particle seeding year (i.e. the particle age) (d). For all metrics except transport distance, modelled sink particles of supraglacial origin tend to display higher median values (orange bars taller than blue bars), suggesting that, on average, they tend to be older (i.e. seeded earlier), spend more time in glacier ice, and spend more time in ice-free conditions during their source-to-sink journey, relative to sink particles of subglacial origin.

### 3.3.3 Addressing ‘sink-to-source’ debates: The Mont Salève erratics case study

To demonstrate that our modelled glacial sediment trajectories can help address tangible research questions and scientific debates in the Alps, we conduct a specific analysis for the example of the Mont Salève erratics. The Mont Salève, located 10 km to the south of Geneva, is a ~600 m tall, ~16 km long, and ~2.5 km wide limestone mountain part of the Jura Massif. The Salève features a flat plateau-like summit (~1300 m a.s.l.) displaying approximately 400 preserved erratic boulders (1200 pre-exploitation) officially protected since 1877 and subject to investigations since (e.g. Coutterand, 2010). Some of the erratics were geologically identified as Gneiss from the Siviez-Michabel nappe (Valais, Switzerland) while



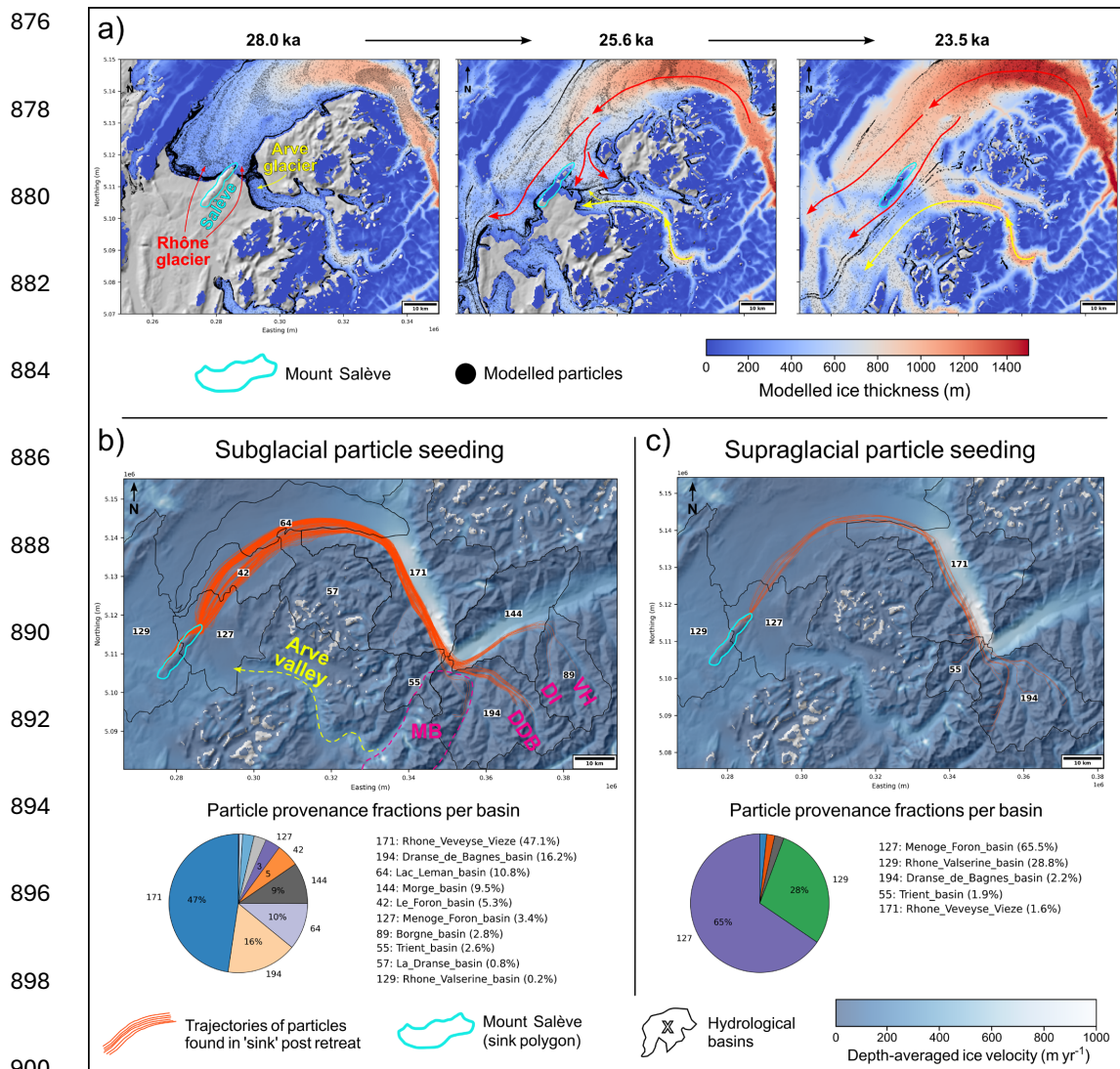
840 others as Mont-Blanc granite. They were hypothesised to have been deposited during retreat phases and  
842 thinning from the largest Late-Pleistocene glaciations of the AIF. More specifically, Coutterand (2010)  
844 attributed their glacial transport and deposition to two separate glacier systems; i) the Rhône glacier  
846 flowing along the Rhône valley and Geneva Lake basin thus reaching the Salève from the northeast, and  
848 ii) the Arve glacier flowing along the Arve valley and originating from the Mont-Blanc Massif thus  
850 reaching the Salève from the southeast. Our study enables to compare these hypotheses against modelled  
852 estimates for the first time. Firstly, our results suggest the Mont Salève summit was covered by a thin (~30  
854 - 100 m) layer of ice during the LGM, when peak AIF extent and volume was reached (~24.8 ka; Leger et  
856 al., 2025) (Fig. 8). When tracking the trajectories of all particles deposited on the Mont Salève following  
deglaciation, we find that no particles are modelled to be deposited by the Arve glacier (Fig. 8). Instead,  
between 40 and 18 ka, 100% of modelled ice-contact deposits on the Salève are deposited by the Rhône  
glacier, with glacial sediment travelling exclusively along the western side of the Rhône valley and the  
southern side of the Geneva Lake basin (Fig. 8). The seeding locations of particles deposited on the Salève  
trace back to the northeastern sectors of the Mont-Blanc Massif, thus overlapping Mont-Blanc granite  
outcrops, but also to the Dranse de Bagnes, Dixence, and Val-d'Hérens valleys (Vallais, Switzerland) thus  
overlapping the Siviez-Michabel gneiss nappe (Bigi et al., 1990) (Fig. 8). Thus, in our simulations, the  
geographical origin of both subglacially- and supraglacially seeded particles can explain the lithologies of  
erratic boulders found on the Salève plateau (Fig. 8).

858 The lack of Salève-deposit trajectories associated with the Arve glacier is related to the modelled dynamics  
of confluence between the Rhône and Arve glaciers. Our simulations suggest that during the last AIF  
860 advance preceding the LGM (~28-26 ka), a branch of the more voluminous and thicker Rhône glacier  
862 expanded southward from the Geneva Lake basin into the Arve valley and around the southeastern flanks  
864 of the Salève. This modelled expansion generates enough driving stress to push the thinner Arve glacier,  
866 forced to redirect its flow south-westward due to its lower ice discharge rate (Fig. 8). Consequently, our  
868 simulations suggest the Mont Salève remained surrounded by ice exclusively from the Rhône glacier  
870 during the LGM and until final deglaciation from the area (~20 ka in our simulations). More empirical  
investigations and dating of the Salève erratics are needed to either validate or discard this new model-  
derived hypothesis, which differs from the previous empirical hypothesis (Coutterand, 2010). Regardless,  
this study case of the Mont Salève erratics is a prime example demonstrating how Alps-wide modelling  
of glacial sediment transport can help address questions on past glacier flow dynamics and the former  
transport history of certain ice-contact deposits.

872

874





902 **Figure 8. Instructed Glacier Model (IGM) output, sink particle trajectory maps, and sink particle provenance**  
 904 **fractions per hydrological basin, for the Mont Salève erratics case study (see section 3.3.3). The three ice-**  
 906 **thickness model output snapshots (a) at 28, 25.6, and 23.5 ka display the modelled ice thickness fields in the**  
 908 **region of the Mont Salève indicating how the Rhône and Arve glaciers interact in our model. More**  
 910 **specifically, they show how, in our simulation, the Rhône glacier pushes the ice from the Arve glacier towards**  
 912 **the southwest forcing it to redirect its flow: causing the Mont Salève to be surrounded by modelled ice**  
 914 **exclusively from the Rhône glacier during the entire Last Glacial Maximum (LGM). This in turn explains**  
 916 **the resulting particle glacial-transport trajectories (b, c), highlighted by orange lines, shown for particles**  
**ending up on and around the Mont Salève following final ice retreat. These suggest no ice-contact deposits of**  
**the Mont Salève are modelled to be transported by the Arve glacier. They are instead all exclusively**  
**transported by the Rhône glacier. Note particle seeded within Basin 129 (28% of particles for supraglacial**  
**seeding) are only local to Mont Salève: i.e. particles from near the summit moved downslope and which still**  
**end up within the mapped polygon following final ice retreat. On panel b; ‘MB’, ‘DDB’, ‘DI’, and ‘VH’ stand**  
**for the ‘Mont-Blanc Massif’, and the ‘Dranse de Bagnes’, ‘Dixence’, and ‘Val-d’Hérens’ valleys, respectively,**  
**enabling to locate places mentioned in main text (section 3.3.3).**



918

### 3.4 The source-to-sink analysis and catalogue

920

With the source-to-sink analysis, we produce a second catalogue of time-transient (40-18 ka) glacial sediment trajectories for a selection of key surface lithologies across the Alps, hereafter referred to as our 'sources' (see section 2.4) (link: <https://doi.org/10.5281/zenodo.18374156>). These trajectories reveal the pathways of particles seeded either subglacially or supraglacially within source polygons ( $n = 22$ ; Fig. 3b). For each source polygon and seeding type, we provide a high-resolution map of source particle trajectories. We interpret these source-to-sink trajectories as model estimates of possible locations (along the modelled trajectories) where sediments of a specific surface lithology may have been transported to and deposited by ice between 40 and 18 ka. These locations can then be compared against the coordinates of documented deposits (e.g. erratic boulders) of known lithology, which may help assess the accuracy of our modelling.

#### 3.4.1 A source-to-sink case study: the 'Arolla Gneiss' trajectories

As an example from our catalogue, we here describe our source-to-sink analysis for a single lithology, i.e. Arolla Gneiss (source number 4 in the catalogue: Fig. 9). This lithology is part of the Austroalpine system of the western Alps and, more specifically, of the Dent Blanche and Sesia Lanzo composite nappe-system of Paleoafrican provenance (Manzotti, 2011). It was formed during the Early-Alpine and Lepontine tectonometamorphic events and is mainly composed of greenschist orthogneisses from Late-Hercynian granitoids (Bigi et al., 1990a). This lithology outcrops mainly within the Dent Blanche, Dent d'Hérens and Weisshorn Massifs (Swiss Alps), and along a narrow band of the southern Italian Alps stretching for ~160 km from the Valle di Viù to the Melezza valley and Locarno (Ticino, Switzerland) (Fig. 9). Numerous erratics deposited in the Swiss and Italian alpine forelands are of Arolla-Gneiss lithology (e.g. Graf et al., 2015).

944

In our simulations, Arolla Gneiss is modelled to be eroded and transported by ice into vastly different valleys and outlet glacier catchments following diverse and complex trajectories (Fig. 9). It is for instance modelled to be transported by the Rhône outlet glacier reaching the Lyon outlet glacier (France), but also by the Solothurn outlet glacier (Switzerland), the Dora Baltea outlet glacier reaching the Ivrea morainic arc (Italy), and the Ticino-Toce outlet glacier (Italy) (Fig. 9). Arolla Gneiss trajectories enable us to visualize how modelled ice flux from the upper Rhône glacier diverges over the northern Lake Geneva flanks during the LGM, as previously modelled (e.g. Juvet et al., 2017). Indeed, it reveals how modelled ice flowing along the true right side of the Rhône valley (between Martigny and Montreux, Switzerland) bends eastwards and heads towards Solothurn, while ice flowing along the true left side of the Rhône valley bends south-westwards along the Geneva Lake and heads towards the Lyon outlet glacier (Fig. 9).



956 Interestingly, some of the particles heading towards Solothurn are pushed against the southeastern Jura  
flanks in locations of modelled ice transfluences causing glacial transport through the Jura mountains, into  
958 the Doubs valley and towards the northern margins of the Jura icecap (France) (Fig. 9). Our simulations  
thus produce transfluences of alpine ice overflowing the Jura mountains during peak LGM extent and  
960 volume (~24.8 kyr). These transfluences are modelled in three broad locations, firstly towards the Vallorbe  
pass and the valley of the Jougne (46°43'N; 6°23'E), secondly towards Baulmes and Sainte-Croix (East  
962 of the Mount Suchet: 46°48'N; 6°30'E), and thirdly directly West of Vallorbe over the 'Grotte aux Fées'  
cave and the Combe du Puits area (46°42'N; 6°19'E). Former expansions of alpine glaciers overflowing  
964 the Jura mountains are thought to have occurred during pre-LGM maximum Late-Quaternary glaciations  
such as during Marine Isotope Stage (MIS) 12, 10, 8, or 6 (Keller and Krayss, 2011; Preusser et al., 2011;  
966 Graf et al., 2015). However, no published evidence yet exists for such transfluences during the LGM (MIS  
2) (Campy, 1992; Buoncristiani & Campy, 2011). Our model may either slightly overestimate ice thickness  
968 over the Rhône and Solothurn glaciers during the LGM, or may be correct but sedimentological evidence  
for such momentary transfluence may be rare and not yet documented/dated. The modelled Arolla-Gneiss  
970 trajectories reveal other surprising and complex pathways, such as possible transport of glacial sediments  
up into the Aulps valley (Morzine river valley, France) by ice from the Rhône glacier which, in our model,  
972 generates southward ice-flow upvalley from the Geneva Lake basin (Fig. 9). Key differences can be  
observed between modelled Arolla-Gneiss trajectories of particles seeded subglacially versus  
974 supraglacially. Within the Rhône glacier catchment, Arolla-Gneiss outcrops are confined to high-elevation  
topographies located towards the glacier's upper accumulation zone, where nunatak occurrence and  
976 rockfall potential are high, and where modelled basal ice velocities remain relatively low (<50 m yr<sup>-1</sup>).  
Thus, within the Rhône glacier catchment, supraglacially seeded particles from Arolla-Gneiss outcrops  
978 yield a higher number and diversity of modelled trajectories, relative to subglacially-seeded particles (Fig.  
9). In the southern Italian Alps, particle trajectories show the opposite, with numerous outcrops located in  
980 fast-flowing ice regions leading to higher numbers of trajectories and ice-contact deposit locations for  
particles of subglacial origin.

982

984

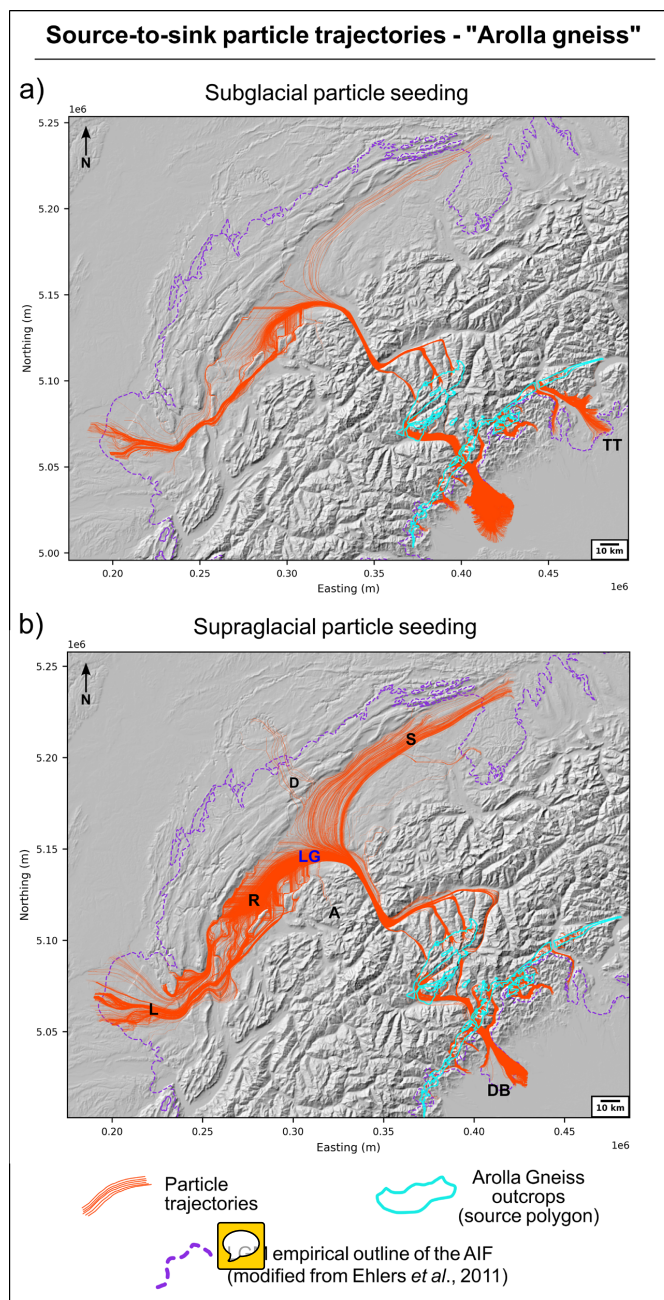
986

988

990



992  
994  
996  
998  
1000  
1002  
1004  
1006  
1008  
1010  
1012  
1014  
1016  
1018  
1020



1022 **Figure 9. Source-to-sink analysis and resulting particle glacial-transport trajectories for all particles seeded**  
1024 **within an example source polygon; in this case a single surface lithology from our source-to-sink catalogue**  
1026 **(n=22 surface lithologies), i.e. the Arolla Gneiss (originally mapped by Bigi *et al.*, 1990). Particle trajectories**  
1028 **are shown for both subglacial (a) and supraglacial (b) seeding. We interpret these source-to-sink trajectories**  
1030 **as model estimates of possible locations (along the entire trajectories) where ice-contact deposits of the Arolla-**  
**gneiss lithology may have been transported to and deposited by glaciers between 40 and 18 ka (time frames**  
**of simulations). The labels ‘A’, ‘DB’, ‘D’, ‘L’, ‘LG’, ‘R’, ‘S’, ‘TT’ stand for: ‘Aulps valley’, ‘Dora-Baltea**  
**outlet glacier’, ‘Doubs valley’, ‘Lyon outlet glacier’, ‘Lake Geneva’, ‘Rhône glacier’, ‘Solothurn outlet**  
**glacier’, ‘Ticino-Toce outlet glacier’, respectively, and relate to places/features mentioned in the main text**  
**(section 3.4.1).**



1032

#### 3.4.2 Model-data comparison with dated erratics

1034

Our ‘source-to-sink’ analysis provides the opportunity to test model agreement against data from ice-  
1036 contact deposits of known provenance. Here, we conduct such a model-data comparison by compiling  
peer-reviewed publications which dated erratic boulders in the Alps to the time range of our simulations  
1038 (40-18 ka) using terrestrial cosmogenic nuclide exposure dating (Table S1). The compiled erratics need to  
feature a lithological description that is specific enough (e.g. ‘Central Aar granite’) to be associated to a  
1040 well-defined and spatially restricted lithology (unlike ‘limestone’, for instance). Moreover, only one  
sample per location (i.e. a sampling site in original studies) is considered for this test, to reduce statistical  
1042 biases. A total of 38 erratic boulders were found to match these requirements, published in 13 separate  
studies (Ivy-Ochs et al., 2004; Gianotti et al., 2008; Reber et al., 2014; Graf et al., 2015; Bichler et al.,  
1044 2016; Wüthrich et al., 2018; Ivy-Ochs et al., 2018; Boxleitner et al., 2019; Prud’homme et al., 2020;  
Braakhekke et al., 2020; Kamleitner et al., 2022; Kamleitner et al., 2023; Roattino et al., 2023). Exposure  
1046 ages were re-calculated consistently as part of the AlpIce geochronological database (Kamleitner et al., *in  
prep*). Modelled particle trajectories (subglacial and supraglacial seeding combined) for the relevant  
1048 source lithology successfully overlap the locations of erratic boulders of that lithology in 26 out of 38  
cases (Table S1). The trajectories thus fit empirical data in 68% of cases. This number would moreover  
1050 increase to 81% would we tolerate a small (<4 km) increase in ice extent in locations where our model  
slightly underestimates ice extent during the LGM, relative to mapped terminal moraines (see Fig. 1a, 4a  
1052 in Leger et al., 2025). Thus, clear model-data misfit is only observed in 18% of cases (10 boulder samples).  
These results suggest our LGM model of the AIF coupled with our particle-seeding and 3D tracking  
1054 schemes can transport particles to appropriate locations, for the majority of the compiled erratics (Table  
S1).

1056

#### 3.5 Detecting LGM ice transfluences across the Alps

1058

As shown above with the example of Arolla Gneiss ‘source-to-sink’ trajectories overflowing the Jura  
1060 Massif, the coupling of 3D particle tracking enables us to estimate, for the first time, the precise locations  
and time span of ice transfluences in the Alps during the LGM (Fig. 10). Ice transfluences occur when the  
1062 growth of ice sheets and/or icefields cause the formation of topographically uncoupled ice domes, i.e.  
which accumulate away from summits and hydrological catchment divides. If the surface elevation of  
1064 these domes exceeds the altitude of neighbouring cols, uncoupling from main hydrological catchments  
occurs causing ice-flow to cross main hydrological divides (Linton, 1949). This can result in glacial  
1066 sediment transport over high-elevations ridges/cols and into different catchments (Monegato et al., 2022)  
(Fig. 10). Reconstructing LGM transfluences can thus help understand former ice-flow dynamics and  
1068 unravel the puzzling lithologies/provenances of certain ice-contact deposits in the Alps (e.g. Reitner et al.,



2010). Here, we loaded our modelled particle trajectories and thus 3D ice-flow lines into a geographic  
1070 information software (ArcGIS Pro 3.4) to detect the occurrence of ice transfluences in our simulations,  
focusing only on the 11 largest hydrological catchments of the Alps (Rhône, Aare, Rhein, Isar, Inn, Enns,  
1072 Drau, Piave, Brenta, Adige, Po) (Lehner & Grill, 2013). We present this analysis' results in a series of  
maps (Figures S8-14) highlighting the locations of modelled ice domes, flowlines, and ice transfluences  
1074 across the Alps. Figure 10 shows one of these maps for the example region of the upper Inn catchment.  
There, the build-up of the 'Engadin' ice dome centred towards Zernez (46°41'N, 10°05' E, 1465 m a.s.l.)  
1076 and reaching a modelled maximum ice surface elevation of ~3100 m a.s.l. leads to a complex network of  
topographically uncoupled flowlines causing a high concentration of ~30 ice transfluences into the  
1078 adjacent Rhein, Adda, Adige, and Isar catchments (Fig. 10). This causes, for instance, modelled ice from  
the Inn valley between St.-Moritz (46°29'N; 9°50'E) and Zernez (a 45 km stretch) flowing south-  
1080 westwards over the Maloja pass (46°24'N; 9°41'E) into the Val Bregaglia, Como Lake basin, and feeding  
the Adda and Seveso outlet glaciers (sinks 2 and 44 in 'sink-to-source' catalogue). As another example,  
1082 we note that our model reproduces the well-documented Simplon pass transfluence (e.g. Florineth &  
Schlüchter, 1998; Kelly et al., 2004; Dielforder & Hetzel, 2014), with ice possibly transporting sediments  
1084 from the Eiger-Mönch-Jungfrau mountains (e.g. Aar granites) across the Rhône valley, over the Simplon  
pass, and into the Ticino-Toce glacier system during the LGM (sink 48 in 'sink-to-source' catalogue,  
1086 Figure S11). In our simulations, we also find that modelled ice is nearly always warm-based towards the  
main ice domes and transfluences occurring during the LGM (see Fig. 6b in Leger et al., 2025). Moreover,  
1088 the modelled time span of transfluence occurrence is highly case-specific and can vary from 1-3 kyr, thus  
only during peak LGM conditions up to nearly the full simulation time frame (i.e. 22 kyr) and LGM  
1090 period (e.g. the Engadin ice dome, Fig. 10). Consequently, our results show that coupling 3D Lagrangian  
particle tracking to glacier evolution modelling can also help identify the detailed events of complex and  
1092 momentary topographic uncoupling of ice-flow during major Quaternary glaciations of the Alps.

1094

1096

1098

1100

1102

1104

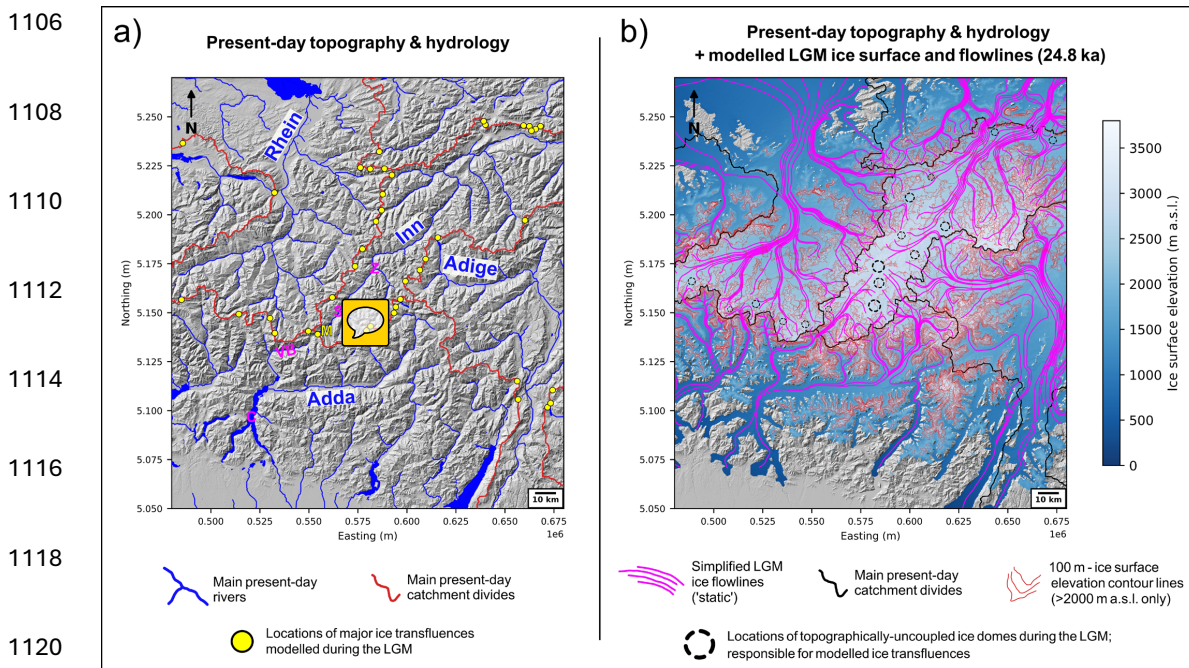


**Figure 10. Map of modelled ice surface elevations and simplified ‘static’ ice flowlines (pink lines) during the LGM (~24.8 ka) in the region of the Engadin ice dome, with locations of modelled ice transfluences (yellow dots on panel a). These transfluences can explain the complex provenance of certain ice-contact deposits. We quantified them for the 11 largest river catchments of the Alps, whose divides are shown in red on panel a, and black on panel b. A series of six figures displaying the same ice-transfluence analysis for five other regions of the Alpine Ice Field (AIF) are available in the Supplementary Materials. Note that whilst useful for the visual purpose of this figure, the simplified glacier flowlines (pink lines) shown here (panel b) are drawn from so-called ‘static’ flowlines, which are non-time-transient and only obtained from the depth-averaged ice velocity field modelled during a single time frame: i.e. the maximum AIF volume; at 24.8 ka. These should only be considered useful to visualize the modelled flow direction of ice at the precise locations of transfluences and only during peak LGM. The substantially more complex and accurate time-transient flow trajectories obtained from our 3D Lagrangian particle tracking, displayed in Figures 6 and 9 for example, are more diverse and representative of the modelled time-transient ice-flow trajectories, but would make visualizing transfluences on this figure impossible given the large number of modelled particles and resulting cross-cutting trajectories (see Figure S7). On panel a, the ‘C’, ‘M’, ‘S’, ‘VB’, and ‘Z’ labels stand for ‘Lake Como’, ‘Maloja pass’, ‘St. Moritz’, ‘Val Breglaglia’, and ‘Zernez’, respectively, and relate to locations mentioned in main text (section 3.5).**

### 3.6 Particle trajectory sensitivity to model parameters

To assess the sensitivity of our particle trajectories to both the seeding scheme and model parameters, we conduct two additional AIF simulations that differ from the original setup presented above like so: i) The first sensitivity test uses a ‘simple’ seeding scheme, which is not process-based and instead creates particles supraglacially in a spatially- and temporally-regular manner, i.e. with seeding occurring in 20% of grid cells exclusive to the accumulation zone, and regularly every 300 yrs. ii) The second sensitivity



1148 test uses the same ‘complex’ seeding as the original scheme (Fig. 2) but employs the parameter values of  
1150 a different ensemble simulation (i.e. number 24) within the set of 8 Not-Ruled-Out-Yet simulations  
1152 obtained by Leger et al. (2025). Whilst featuring different ensemble-varying parameter values (see Table  
1154 S1 in Leger et al., 2025), simulation 24 produces Alps-wide model-data agreements in LGM ice extent  
1156 and thickness that are indistinguishable from simulation 37 (used throughout this study). Input parameter  
differences (n=10) however generate changes in SMB, the basal sliding parameterization, ice rheology,  
and the magnitude of isostatic deflection. Importantly, simulation 24 uses a different bed topography than  
simulation 37, with no removal of valley-fill sediments.

1156

In the first sensitivity test, which uses ‘simple’ seeding instead, model agreement with the locations of  
dated erratics presented above (section 3.4.2), using our source-to-sink analysis, decreases from 81-68%  
to 74-58%. These two ranges represent whether we tolerate the small (<4 km) increase in ice extent  
mentioned above (section 3.4.2). Whilst not substantial, this decrease in model-data agreement is  
noticeable and suggests that a less process-based particle seeding scheme leads to a worse model-data fit  
on the provenance, glacial transport, and deposition histories of ice-contact deposits during the LGM. In  
the second sensitivity test, as the seeding scheme is unchanged from the original (see section 2.2), we can  
use provenance fractions (%) per hydrological basin (n=241) for each sink (see section 2.4) to quantify  
inter-simulation differences. Here, when using parameters from Leger et al. (2025)’s ensemble simulation  
24 instead of 37, we find that particle provenance fractions per hydrological basin (e.g. percentages in  
Figs. 6, 8) remain identical in ~72% of cases, on average (median difference: 28.5%). When comparing  
particles’ provenance basins irrespective of fraction percentages, we find sink particles originate from the  
same basins in 88.5% of cases. Thus, running a simulation which yields a similar LGM model-data fit but  
uses different sensitive parameter values causes sink particles to originate from different basins in 11.5%  
of cases and provenance fractions to vary by 28.5% on average. These results show a non-negligible inter-  
simulation variability highlighting a noticeable sensitivity of particle trajectories and provenances to  
modelled ice dynamics and/or bed topography changes. However, this test also shows that the majority of  
particle trajectories, provenances, and glacial transport histories remain unchanged relative to the original  
simulation.

1176

## 1178 4 Discussion



### 1180 4.1 Limitations and future work

1182 The computational gains of GPU-based glacier modelling coupled with 3D Lagrangian particle tracking  
enabled us to produce, for the first time, an Alps-wide estimation of transient glacial sediment pathways  
1184 during the last glaciation (40-18 ka). Although our model-data comparison of source-to-sink trajectories



1186 yields promising results with between 81% and 68% model fit with dated erratics' locations (section 3.4.2,  
1187 Table S1), this study should be considered a first-order attempt yielding limitations and room for  
1188 improvement. We here describe the main limitations of the assumptions made in this experiment,  
1189 providing suggestions for improvement in future modelling work of similar nature.

1190 In this study, we assume passive particle glacial transport with no interaction with ice rheology and flow  
1191 dynamics. In reality, supraglacial debris can influence glacier surface mass balance through insulation  
1192 (e.g. Rowan et al., 2015) while basal ice sediments can alter basal friction and thus glacier sliding  
1193 velocities (Hallet, 1981; Iverson et al., 2003). Our modelling also assumes all glacial sediment to move at  
1194 the same velocity as the ice. Whilst this is a common modelling assumption (e.g. Rowan et al., 2015;  
1195 Jouvét et al., 2017; Bernard et al., 2020; Margirier et al., 2025), the drag force in Stokes Law can cause  
1196 resistance and lower velocities for clasts advected within highly viscous fluids (e.g. ice; Byers et al., 2012).  
1197 Moreover, complex mechanisms of sediment storage occur (e.g. lodgement tills) at partially coupled ice-  
1198 bed interfaces causing sediment advection speeds below ice velocity (Alley et al., 1997; Evans et al.,  
1199 2006). On the contrary, gravitational and fluvio-glacial transport within glacier systems can generate  
1200 sediment advection speeds greater than ice velocity (Walder and Fowler, 1994). Gravitational englacial  
1201 transport also occurs when a glacier features numerous fractures in which debris can fall, a mechanism  
1202 that is not yet modelled in glacier-wide simulations. Sediment transport by rivers (proglacial) and  
1203 subglacial drainage, whilst not modelled in this study, can also complexify deposits' transport histories by  
1204 moving large sediment volumes further down-river prior to glacier re-entrainment (Lane et al., 2017). In  
1205 future work, modelling these complex mechanisms would require full coupling of both subglacial  
1206 hydrology and sediment-transport modules to glacier-evolution models (Delaney et al., 2023).

1208 We assume all sediment to be fully preserved during glacial transport, and that variability in ice-contact  
1209 deposit provenance is exclusively controlled by variations in seeding and glacial transport histories.  
1210 However, clast erosion during glacial transport also plays an important role. Indeed, glacial sediments  
1211 transported over greater distances are more likely to spend time at the ice-bed interface where they  
1212 typically undergo abrasion, crushing, or truncation (Boulton, 1978). With increasing time and transport  
1213 distance, this can generate rounding and comminution of coarse sediments (e.g. boulders, cobbles) into  
1214 finer fractions (e.g. silts, sands and gravels) which can be mobilized by subglacial hydrology and  
1215 evacuated downstream. Subsequently, the likelihood of finding sediments from a specific source in ice-  
1216 contact deposits tends to decrease with increasing distance from that source (Humlum, 1985). In future  
1217 modelling work, more realistic provenance fractions may thus be obtained through parameterizations that  
1218 reduce particle preservation as glacial transport time and distances increase.

1220 Our particle seeding scheme assumes that all bed surfaces are equally susceptible to subglacial erosion  
1221 and production of supraglacial debris via gravitational mass wasting. This is a simplification as different



1222 lithologies yield different hardnesses and varying susceptibilities to abrasion, plucking, frost shattering,  
1224 weathering, and other erosion mechanisms (Moosdorf et al., 2018). The subglacial erosion susceptibility  
1226 of distinct outcrops is also often dependent on local tectonic pre-conditioning (e.g. degree of rock faulting  
1228 and fracturing). The accuracy of future coupled glacier-particle modelling may thus be increased by adding  
an erodibility index parameter controlling the seeding likelihood based on rock hardness, faulting,  
temperature-driven rock-permafrost conditions, and resistance to erosion, constrained by present-day  
geological observations and/or reconstructed past erosion rates (Gallach et al., 2021).

1230 Soft beds under temperate glaciers can become saturated with meltwater, leading to reduced effective  
1232 pressure, lower basal yield stress, and faster sliding velocities (Iverson et al., 1995). While a meltwater  
1234 feedback on sliding is included in our thermo-mechanically coupled glacier model setup (Leger et al.,  
2025), we consistently assume a positive correlation between sliding velocities and subglacial particle  
seeding through abrasion and plucking (Fig. 2). However, this may not always be the case as water  
saturation of soft beds and reduced effective pressure can instead shield bed material from  
abrasion/plucking reducing sediment mobilization or causing local soft bed deformation to instead  
dominate (Boulton, 1979).

1238

Finally, while our GPU-based approach enables us to track an unprecedented number of particles in ice  
1240 (~20.5 million) given our simulations' spatio-temporal scales, sediments are ubiquitous in real glaciers.  
Therefore, our modelling, which also does not include the re-mobilization by glaciers of pre-LGM  
1242 sediment deposits, likely still underestimates the diversity of pathways glacial sediments may follow  
within a glacier system as complex as the former AIF during Late-Quaternary glaciations. However, as  
1244 shown with this work, GPU-computing enables coupled glacier-particle modelling to become orders-of-  
magnitude cheaper and more computationally efficient. This should motivate new modelling studies of  
1246 this nature to include the tracking of large particle numbers, thus helping to identify the particle numbers  
that more fully represent the ubiquitous nature of glacial sediments within icefield and ice-sheet systems.

1248

Given the limitations summarized above, it is clear our modelling does not fully capture the complexity  
1250 of glacial sediment sourcing and transport on multi-millennial, Alps-wide scales. Therefore, the diversity  
of 1) provenances and glacial transport pathways for a given ice-contact deposit, and 2) possible ice-  
1252 contact deposit locations for a given source lithology, are likely underestimated by our 'sink-to-source'  
and 'source-to-sink' analyses (e.g. Figs. 6, 9). However, we believe that our simulations still capture the  
1254 majority of former glacial sediment transport pathways, as evidenced by the relatively good model-data  
fit obtained (81-68%) when comparing modelled particle trajectories for a given lithology with data on  
1256 LGM-dated erratic locations (section 3.4.2, Table S1).



1258 As described above (section 2.4), our sink-to-source analysis uses a subjective set of 49 sink polygons  
1260 (Fig. 3a) covering the space between maximum time-independent margins of the modelled AIF and the  
1262 updated LGM empirical outline of Ehlers et al. (2011). Our sink polygons thus result from a consistent yet  
1264 highly simplified Alps-wide separation of large regions containing the LGM margins of former AIF outlet  
1266 glaciers. An obvious future improvement would be to produce a similar sink-to-source analysis for a more  
detailed map of individual glacio-terminal landforms and ice-contact deposits that remain preserved to  
this day, thus enabling a more accurate model-data comparison. However, this would require producing a  
digital (e.g. GIS database), open-access, Alps-wide map of preserved glacial geomorphology with  
geochronological constraints and a consistent naming convention (e.g. Glasser & Jansson, 2008; Clark et  
al., 2018). To our knowledge, such a valuable product is not yet available for the European Alps.

1268

## 4.2 Coupled glacier-particle modelling; wider implications and perspectives

1270

### 4.2.1 New perspectives for paleo glacier model-data comparisons

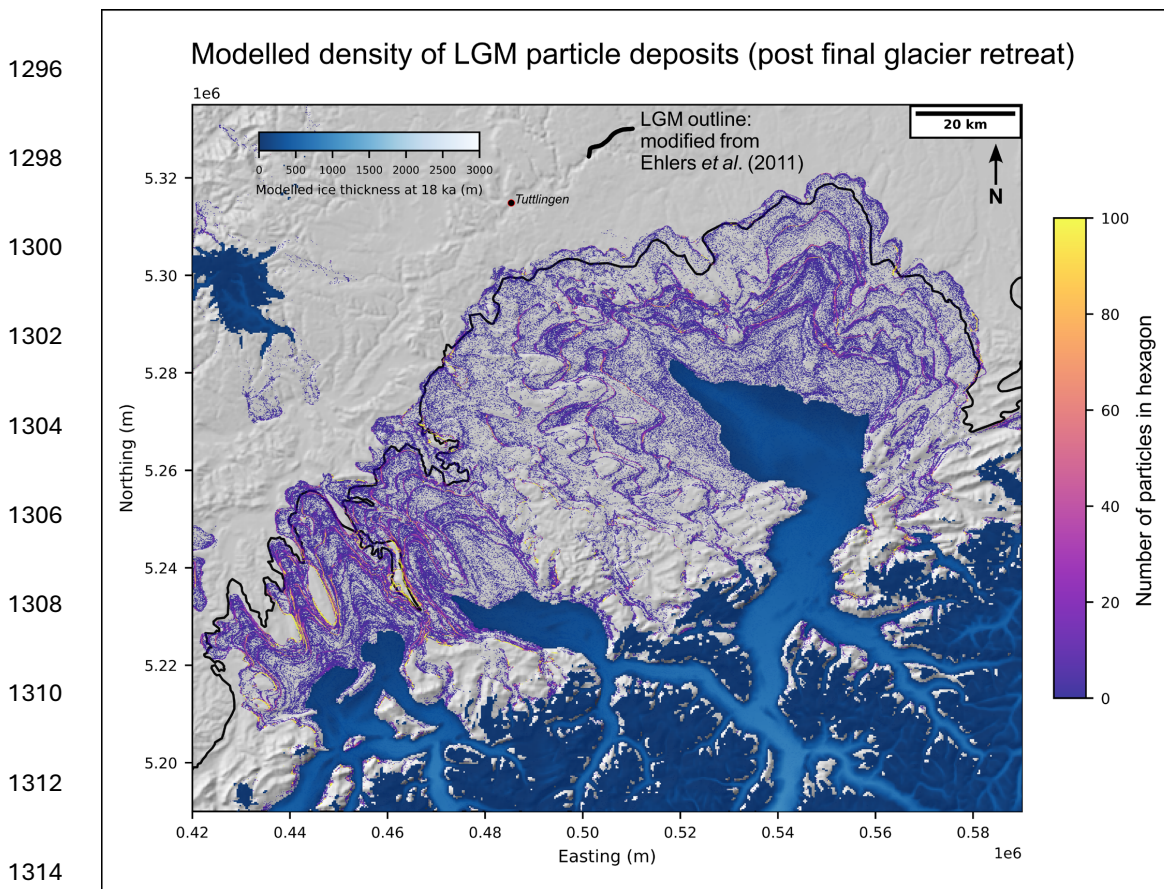
1272

1274 After modelling the final retreat of the AIF from its LGM margins (24-18 ka), our particle advection  
1276 scheme deposits static particles in deglaciated regions which form moraine-like shapes (e.g. Fig. 11,  
Figures S3-6). The resulting spatial densities and shapes of these particle deposits are controlled by; 1) the  
1278 modelled ice-margin shape and location at a given time, 2) the modelled ice margin retreat rate and  
residence time during maximum glacier extent, still-stands, and/or smaller re-advances, and 3) the supply  
of ice-advected particles to the glacier margins at a given model location and time. To improve the  
accuracy of the model regarding these three mechanisms, one could compare the spatial patterns of  
modelled particle deposits against the preserved glacio-geomorphological record (Fig. 11, Figures S3-6).  
Although this is not within the scope of this study, we believe this work opens the possibility to design  
new post-processing tools to automatically quantify the agreement between modelled particle deposits  
(post deglaciation) and preserved landforms such as terminal and lateral moraines. This could represent a  
novel approach to paleo model-data comparison that may complement existing tools (e.g. Ely et al., 2019;  
Archer et al., 2023, Veness et al., 2025) designed to automatically score transient paleo simulations and  
quantitatively evaluate model sensitivities to - and the adequacy of - input parameterizations and climate  
forcings (Fig. 11). Such comparison may also help identify mechanisms controlling the spatial  
heterogeneity of preserved ice-contact deposits found across deglaciated forelands and valleys today (Ivy-  
Ochs et al., 2022).

1290

1292

1294



1316 **Figure 11.** Map of modelled particle deposit densities located in modelled ice-free regions at 18 ka, the final  
1318 timestep of our Alpine Ice Field (AIF) simulations of the Last Glacial Maximum (here 40–18 ka), and for the  
1320 foreland region of the Rhein, Linth, and Reuss outlet glaciers. The AIF model output is displayed using  
1322 modelled ice thickness at 18 ka. The particle deposit data shown here combines both datasets of particles  
1324 seeded subglacially and supraglacially and is expressed as a spatial density map. Each colored dot is a small  
1326 hexagon in which the total number of deposited particles is computed. Bright yellow colors indicate hexagons  
1328 holding the highest concentrations of deposited particles. This model output clearly highlights periods of  
outlet glacier advances and/or margin stabilization during our AIF simulations through formation of  
moraine-shaped particle deposits. We argue the novel ability to produce such results over large spatio-  
temporal scales with our GPU-based Lagrangian particle tracking coupled to glacier evolution modelling  
may provide room for future model-data comparison exercises that quantify the fit between modelled particle  
deposits and the preserved glacio-geomorphological record (see Discussion section).

#### 1330 4.2.2 A method to investigate complex internal ice-flow dynamics

1332 Lagrangian particle tracking coupled with glacier modelling essentially offers a mechanism to better  
1334 visualize the time-transient 3D flow trajectories of simulated glacier motion (Figure S7). As a result, it can  
help to better understand contemporary and past internal glacier dynamics, including vertical ice motion,



1336 flow convergence and divergence, and the complex behaviours of merging glaciers. Such processes can  
1337 be especially complicated in topographically constrained glacier complexes such as the former AIF. For  
1338 instance, when two glaciers converge, their respective ice masses will become separated by a suture zone  
1339 sometimes visible through formation of medial moraines (Small et al., 1979). Reconstructing the precise  
1340 locations and, importantly, the lateral migrations of such suture zones in paleo glaciers, which result from  
1341 disequilibrium in the magnitudes of confronting driving stresses from two glaciers, can be crucial to  
1342 explain: 1) the formation of specific subglacial landforms and their locations (e.g. lineations, drumlins and  
1343 their orientations), 2) the lack or instead over-abundance of ice-contact deposits in specific locations, or  
1344 3) the puzzling provenances of specific sediments deposited at glacier margins. While such complex ice  
1345 dynamics can be well-represented in glacier evolution models solving high-order ice-flow physics, particle  
1346 tracking offers a means to easily visualize and quantify these processes (otherwise invisible) in model  
1347 outputs. Our Mont Salève case study (section 3.3.3) is a good example for which understanding the  
1348 location and migration of the suture zone separating the Rhône and Arve glaciers, easily visible with  
1349 particles on Figure 8 (panel a), is key in understanding the modelled provenance and transport pathways  
1350 of specific ice-contact deposits in this region (e.g. the Mont Salève erratics).

1350

#### 1351 *4.2.3 Implications for research on glacial landscape evolution*

1352

1353 By combining our results with those of Leger et al. (2025), we demonstrate that GPU-parallelization can  
1354 substantially decrease the computational cost of glacier evolution modelling coupled with Lagrangian  
1355 particle tracking (Fig. 4). Besides helping to estimate glacial sediment transport trajectories over multi-  
1356 millennial and continental spatio-temporal scales, we believe this new approach opens the door to a range  
1357 of earth-surface modelling capabilities that may prove useful in addressing research questions in the fields  
1358 of glaciology and mountain geomorphology. As an example, we believe there is potential for future model-  
1359 data comparison studies to better characterize the role of glacial erosion on the relief development of  
1360 mountain belts during Quaternary glaciations (e.g. Bernard et al., 2025), but also on more contemporary  
1361 timescales (e.g. Delaney et al., 2023). Open questions remain, for instance, regarding the relative  
1362 proportions of glacial erosion materials evacuated as glaciofluvial bed/suspended load versus frozen-on  
1363 englacial debris, their role in controlling sediment export and deposition rates in the lowlands, and the  
1364 spatio-temporal variability of these different processes under changing hydro-climatic conditions (Alley  
1365 et al., 1998; Zhang et al., 2022; Fedotova & Magnani, 2024; Delaney et al., *in press*). Large uncertainties  
1366 remain also regarding subglacial mechanisms of sediment storage and resulting shielding of bedrock  
1367 erosion, introducing sediment evacuation delays that are challenging to quantify, and which may bias  
1368 current understandings of subglacial erosion's correlation with basal glacier conditions including ice  
1369 velocity and temperature (Herman et al., 2021; Delaney & Anderson, 2022). These challenging questions  
1370 would benefit from new model-data comparison studies that bridge spatio-temporal gaps in empirical



1372 observations, thus making more holistic and fully coupled model frameworks involving particle tracking  
valuable tools for future investigations addressing these questions (Delaney et al., 2023).

1374 To this day, one of the most advanced and efficient models coupling glacier-flow simulations with  
1376 processes of fluvial and hillslope erosion, subglacial erosion, subglacial hydrology, and sediment transport  
over multi-millennial timescales, is the integrated second-order shallow ice approximation model  
(iSOSIA; Egholm et al., 2011). However, it remains computationally unfeasible to run such a CPU-based  
1378 model over entire mountain ranges (e.g. the Alps), Quaternary-glaciation timescales ( $10^4$ - $10^6$  yr), and at  
the high spatial resolutions (<500 m) required to accurately resolve steep mountain topographies (Bernard  
1380 et al., 2025). On the other hand, recent advances in GPU-optimized modelling and physics-informed  
machine learning have enabled to overcome such computational bottlenecks whilst in some cases  
1382 respecting high-order 3D physics (e.g. Jouvét & Cordonnier, 2023; Cordonnier et al., 2023; Jain et al.,  
2024; Leger et al., 2025). The efficient GPU-parallelization of Lagrangian tracking will enable  
1384 incorporating end-to-end advection of large particle numbers within fully coupled glacier-and-landscape  
evolution models. Therefore, it seems plausible that over the next few years, GPU-based modelling  
1386 approaches permit high-resolution simulations whose outputs can be directly compared against empirical  
data on, for instance, Quaternary glacier incision rates and timing (e.g. Valla et al., 2011) or sediment  
1388 export volumes and provenance data (e.g. Herman et al., 2015; Koppes et al., 2015; Overeem et al., 2017).  
Such model-data comparisons may shed light on the complex mechanisms influencing the dynamics of  
1390 glacial erosion and its interaction with climate and topographic change over various spatio-temporal  
scales.

1392

1394

## 5. Conclusion

1396

This study presents the first modelling reconstruction of sediment transport by glaciers across the entire  
1398 European Alps during the Last Glacial Maximum (LGM). This is achieved via the new coupling of 3D  
Lagrangian particle tracking within the Graphics Processing Units (GPU)-accelerated, high-resolution  
1400 glacier simulations of Leger et al. (2025) using the Instructed Glacier Model (IGM). Our modelling  
computes the 3D ice advection of tens of millions of particles, enabling us to simulate complex, time-  
1402 transient glacial sediment transport trajectories across the Alps over multi-millennial timescales (40-18  
ka), and at an unprecedentedly high spatial resolution (300 m). Here, a key methodological innovation is  
1404 the development of process-based particle seeding schemes for both subglacial and supraglacial sediment  
origins over large spatial scales, attempting to capture distinct erosion and debris entrainment dynamics.  
1406 Our GPU-based approach significantly reduces the computational cost of Lagrangian tracking, making it



feasible to track tens of millions of particles within glacier evolution models ran over continental domains,  
1408 which represents a computational breakthrough for glacial sediment modelling.

1410 Our two complementary sets of results, i.e. the sink-to-source (reconstructing ice-contact deposit  
provenance) and source-to-sink (mapping potential depositional locations) analyses, yield Alps-wide  
1412 estimates of LGM glacial sediment routing, transport times, erosion timing, and cumulative ice-free  
exposure. The full results of these analyses are presented in two catalogues accessible via the Zenodo  
1414 repository attached to this publication. We find particles of supraglacial origin are typically eroded earlier  
in time (i.e. are older), experience longer glacier residence times, and more cumulative ice-free exposure,  
1416 with implications for interpreting cosmogenic nuclide inheritance signals in surface exposure dating for  
instance.

1418

By presenting case studies such as the Mont Salève erratics transport histories, we also show how our  
1420 modelling can address empirical hypotheses by reconstructing detailed particle trajectories consistent with  
known lithologies, which can in certain cases suggest revised paleo ice-flow interpretations. After  
1422 comparing model results against empirical data, we find that sediment trajectories overlap with dated  
erratic boulders in 81-68% of cases, supporting the reliability of the approach and validating the use of  
1424 process-based particle seeding schemes over simpler methods. Furthermore, our results enable us to  
precisely detect and map multiple LGM ice transfluences, including previously unreported overflow  
1426 pathways, and estimate their occurrence durations, thus offering new perspectives on complex internal  
ice-flow and topographically uncoupled glacier dynamics across the Alps.

1428

We believe this first Alps-wide modelling of LGM glacial sediment transport and ice-flow dynamics  
1430 provides a range of predictions that will prove useful to glacial geologists, geomorphologists,  
sedimentologists and industries studying ice-contact sediments related to Late-Quaternary glaciations of  
1432 the European Alps. Finally, the computationally efficient (GPU-based) coupled glacier-particle modelling  
framework developed here opens new avenues for quantitative model-data comparisons using preserved  
1434 glacial geomorphology and provides a powerful tool to study and better constrain paleo ice dynamics,  
sediment provenance, and Quaternary glacial landscape evolution.

1436

1438

1440

1442



1444 **Code and data availability.**

1446 The data that represent the main findings of this study: namely the ‘sink-to-source’, ‘source-to-sink’, ‘ice-  
1448 transfluence’ data catalogues and their corresponding particle-trajectory polyline shapefiles are available  
1450 from the following Zenodo open-access online repository: <https://doi.org/10.5281/zenodo.18374156>. This  
1452 repository also features a series of videos displaying Alps-wide results from our Instructed Glacier Model  
1454 (IGM) simulations including the visual rendering of particle advection and deposition for both subglacial  
1456 and supraglacial seeding and zoomed in for 10 different regions of the Alps. These videos are also  
accessible via the IGM YouTube channel: <https://www.youtube.com/@IGMGlacierModel/playlists>. Finally,  
this repository also features codes, files and detailed instructions required to reproduce this study’s specific  
IGM simulations using the correct IGM version (2.2.1.). Note that whilst the full modelled particle  
database produced in this study is too large to be stored online and shared (~1.22 TB), readers are  
encouraged to contact the corresponding author if wishing to compute and display particle trajectories for  
specific sinks or sources.

1458 The IGM source code (Python programming language) which now includes the fully GPU-optimized  
particle-tracking module (in IGM versions  $\geq 2.2.3$ ) is open access and available from the GitHub repository  
1460 at <https://github.com/instructed-glacier-model/igm.git>. IGM’s documentation is available from its official  
website at <https://igm-model.org/>.

1462

**Supplement.**

1464 The supplement related to this article is available online at: .....

1466 **Author contributions.**

T.P.M.L., G.J., and M.B. conceived and designed the study with input ideas from S.K., A.V., A.H., F.H.  
1468 and S.N. G.J. developed the original version of IGM, including the Lagrangian particle-tracking module  
in IGM, whose code was then modified and improved by B.F. within the context of this study to become  
1470 fully GPU-optimised, with tests and compute-time diagnostics from T.P.M.L. T.P.M.L. designed and coded  
the particle seeding schemes and carried out the IGM simulations. T.P.M.L. created the post-processing  
1472 coding workflow for particle trajectory extraction and mapping, with help from B.A. who optimized the  
Python code for efficient search of the large output particle database. T.P.M.L. compiled and generated the  
1474 hydrological basin, ice-contact deposit, and surface lithology databases required for running the ‘sink-to-  
source’ and ‘source-to-sink’ analyses presented above. S.K. contributed to the extraction and mapping of  
1476 certain surface lithologies. T.P.M.L. conducted the model-data comparison against erratic boulder data  
leveraging prior literature data mining and exposure-age recalculations from S.K. T.P.M.L. ran model  
1478 sensitivity analyses, wrote the manuscript, and produced all figures and supplementary materials. All co-  
authors contributed to the discussions, interpretations and gave feedback on the final manuscript and  
1480 figures.



1482 **Competing interests.**

The contact author has declared that none of the authors have any competing interests.

1484

**Acknowledgements.**

1486 All IGM simulations were carried out on ‘Octopus’, a local computing cluster at the University of  
Lausanne, Faculty of GeoSciences and the Environnement (FGSE), managed by Dr. Ludovic Raess  
1488 (University of Lausanne) whom we wish to thank for his work and support. We thank Prof. Jean-Luc  
Epard, Prof. Bernhard Salcher, Prof. Franz Neubauer, Dr. Jürgen M. Reitner and Dr. Jean-Daniel  
1490 Champagnac for insightful discussions and for their precious help identifying alpine surface lithologies of  
particular relevance to this work. This work also benefited from discussions with Dr. Remy Veness, Dr.  
1492 Julien Seguinot, Kejdi Lleshi, and Prof. Georgina King, whom we wish to thank.

1494 **Financial support.**

This research was funded by the Swiss National Science Foundation, through a grant (RECONCILE:  
1496 project number: 213077) awarded to G.J, A.V., and S.N.

1498

1500

1502

1504

1506

1508

1510

1512



## 1514 **References**

- 1516 Aaron, J.: ORIN-3D – A new model for efficient simulation of landslide motion on a GPU using CUDA, *Comput. Geotech.*, 153, 105078, <https://doi.org/10.1016/j.compgeo.2022.105078>, 2023.
- 1518 Agassiz, L.: Études sur les glaciers, Aux frais de l'auteur. En commission chez Jent et Gassmann, libraires., Soleure, <https://doi.org/https://doi.org/10.1017/CBO9781139235877>, 1840.
- 1520 Alley, R. B., Cuffey, K. M., Evenson, E. B., Strasser, J. C., Lawson, D. E., and Larson, G. J.: How glaciers entrain and transport basal sediment: Physical constraints, *Quat. Sci. Rev.*, 16, 1017–1038, [https://doi.org/10.1016/S0277-3791\(97\)00034-6](https://doi.org/10.1016/S0277-3791(97)00034-6), 1997.
- 1522 Alley, R. B., Lawson, D. E., Evenson, E. B., Strasser, J. C., and Larson, G. J.: Glaciohydraulic supercooling: a freeze-on mechanism to create stratified, debris-rich basal ice: II. Theory, *Journal of Glaciology*, 44, 563–569, <https://doi.org/10.3189/S002214300002070>, 1998.
- 1524 Archer, R. E., Ely, J. C., Heaton, T. J., Butcher, F. E. G., Hughes, A. L. C., and Clark, C. D.: Assessing ice sheet models against the landform record: The Likelihood of Accordant Lineations Analysis (LALA) tool, *Earth Surf. Process. Landf.*, 48, 2754–2771, <https://doi.org/10.1002/esp.5658>, 2023.
- 1528 Aschwanden, A., Bueler, E., Khroulev, C., and Blatter, H.: An enthalpy formulation for glaciers and ice sheets, *Journal of Glaciology*, 58, 441–457, <https://doi.org/10.3189/2012JoG11J088>, 2012.
- 1530 Benn, D. I., Bolch, T., Hands, K., Gulle, J., Luckman, A., Nicholson, L. I., Quincey, D., Thompson, S., Toumi, R., and Wiseman, S.: Response of debris-covered glaciers in the Mount Everest region to recent warming, and implications for outburst flood hazards, *Earth. Sci. Rev.*, 114, 156–174, <https://doi.org/10.1016/j.earscirev.2012.03.008>, 2012.
- 1532 Bernard, M., Steer, P., Gallagher, K., and Lundbek Egholm, D.: Modelling the effects of ice transport and sediment sources on the form of detrital thermochronological age probability distributions from glacial settings, *Earth Surface Dynamics*, 8, 931–953, <https://doi.org/10.5194/esurf-8-931-2020>, 2020.
- 1536 Bernard, M., van der Beek, P. A., Pedersen, V. K., and Colleps, C.: Production and Preservation of Elevated Low-Relief Surfaces in Mountainous Landscapes by Pliocene-Quaternary Glaciations, *AGU Advances*, 6, <https://doi.org/10.1029/2024AV001610>, 2025.
- 1540 Bichler, M. G., Reindl, M., Reitner, J. M., Drescher-Schneider, R., Wirsig, C., Christl, M., Hajdas, I., and Ivy-Ochs, S.: Landslide deposits as stratigraphical markers for a sequence-based glacial stratigraphy: a case study of a Younger Dryas system in the Eastern Alps, *Boreas*, 45, 537–551, <https://doi.org/10.1111/bor.12173>, 2016.
- 1542 Bigi, G., Castellarin, A., Coli, M., Dal Piaz, G. V., Sartori, R., Scandone, P., and Vai, G.: Structural Model of Italy scale 1:500,000, sheet 1, Florence, 1990a.
- 1544 Bigi, G., Castellarin, A., Coli, M., Dal Piaz, G. V., and Vai, G.: Structural Model of Italy scale 1:500,000, sheet 2, Florence, 1990b.
- 1546 Blatter, H.: Velocity and stress fields in grounded glaciers: a simple algorithm for including deviatoric stress gradients, *Journal of Glaciology*, 41, 333–344, <https://doi.org/10.3189/S002214300001621X>, 1995.
- 1548 Boulton, G. S.: Boulder shapes and grain-size distributions of debris as indicators of transport paths through a glacier and till genesis, *Sedimentology*, 25, 773–799, <https://doi.org/10.1111/j.1365-3091.1978.tb00329.x>, 1978.
- 1550 Boulton, G. S.: Processes of Glacier Erosion on Different Substrata, *Journal of Glaciology*, 23, 15–38, <https://doi.org/10.3189/S0022143000029713>, 1979.
- 1552 Boulton, G. S.: Theory of glacial erosion, transport and deposition as a consequence of subglacial sediment deformation, *Journal of Glaciology*, 42, 43–62, <https://doi.org/10.3189/S0022143000030525>, 1996.



- 1556 Boxleitner, M., Ivy-Ochs, S., Egli, M., Brandova, D., Christl, M., and Maisch, M.: Lateglacial and Early Holocene glacier stages - New dating evidence from the Meiental in central Switzerland, *Geomorphology*, 340, 15–31,  
1558 <https://doi.org/10.1016/j.geomorph.2019.04.004>, 2019.
- Braakhekke, J., Ivy-Ochs, S., Monegato, G., Gianotti, F., Martin, S., Casale, S., and Christl, M.: Timing and flow pattern of the Orta Glacier (European Alps) during the Last Glacial Maximum, *Boreas*, 49, 315–332,  
1560 <https://doi.org/10.1111/bor.12427>, 2020.
- 1562 Bueler, E. and van Pelt, W.: Mass-conserving subglacial hydrology in the Parallel Ice Sheet Model version 0.6, *Geosci. Model Dev.*, 8, 1613–1635, <https://doi.org/10.5194/gmd-8-1613-2015>, 2015.
- 1564 Buoncristiani, J.-F. and Campy, M.: Quaternary Glaciations in the French Alps and Jura, in: Quaternary Glaciations - Extent and Chronology - a closer look, vol. 15, edited by: Ehlers, J., Gibbard, P. L., and Hughes, P. D., 117–126, <https://doi.org/10.1016/B978-0-444-53447-7.00010-6>, 2011.
- 1568 Bussien Grosjean, D., Meisser, N., May-Leresche, S., Ulianov, A., and Vonlanthen, P.: The Morcles microgranite (Aiguilles Rouges, Swiss Alps): geochronological and geochemical evidences for a common origin with the Vallorcine intrusion, *Swiss J. Geosci.*, 111, 35–49, <https://doi.org/10.1007/s00015-017-0282-3>, 2018.
- 1570 Byers, J., Cohen, D., and Iverson, N. R.: Subglacial clast/bed contact forces, *Journal of Glaciology*, 58, 89–98, <https://doi.org/10.3189/2012JG11J126>, 2012.
- 1572 Calov, R. and Greve, R.: A semi-analytical solution for the positive degree-day model with stochastic temperature variations, *Journal of Glaciology*, 51, 173–175, <https://doi.org/10.3189/172756505781829601>, 2005.
- 1574 Campy, M.: Palaeogeographical relationships between Alpine and Jura glaciers during the two last Pleistocene glaciations, *Palaeogeogr. Palaeoclimatol. Palaeoecol.*, 93, 1–12, [https://doi.org/10.1016/0031-0182\(92\)90180-D](https://doi.org/10.1016/0031-0182(92)90180-D),  
1576 1992.
- 1578 Capuzzo, N., Handler, R., Neubauer, F., and Wetzell, A.: Post-collisional rapid exhumation and erosion during continental sedimentation: the example of the late Variscan Salvan-Dorénaz basin (Western Alps), *International Journal of Earth Sciences*, 92, 364–379, <https://doi.org/10.1007/s00531-003-0332-0>, 2003.
- 1580 Champel, B., van der Beek, P., Mugnier, J., and Leturmy, P.: Growth and lateral propagation of fault-related folds in the Siwaliks of western Nepal: Rates, mechanisms, and geomorphic signature, *J. Geophys. Res. Solid Earth*,  
1582 107, <https://doi.org/10.1029/2001JB000578>, 2002.
- 1584 Clark, C. D., Ely, J. C., Greenwood, S. L., Hughes, A. L. C., Meehan, R., Barr, I. D., Bateman, M. D., Bradwell, T., Doole, J., Evans, D. J. A., Jordan, C. J., Monteys, X., Pellicer, X. M., and Sheehy, M.: BRITICE Glacial Map, version 2: a map and GIS database of glacial landforms of the last British–Irish Ice Sheet, *Boreas*, 47, 11–e8,  
1586 <https://doi.org/10.1111/bor.12273>, 2018.
- 1588 Clark, C. D., Ely, J. C., Hindmarsh, R. C. A., Bradley, S., Ignéczi, A., Fabel, D., Ó Cofaigh, C., Chiverrell, R. C., Scourse, J., Benetti, S., Bradwell, T., Evans, D. J. A., Roberts, D. H., Burke, M., Callard, S. L., Medialdea, A., Saher, M., Small, D., Smedley, R. K., Gasson, E., Gregoire, L., Gandy, N., Hughes, A. L. C., Ballantyne, C.,  
1590 Bateman, M. D., Bigg, G. R., Doole, J., Dove, D., Duller, G. A. T., Jenkins, G. T. H., Livingstone, S. L., McCarron, S., Moreton, S., Pollard, D., Praeg, D., Sejrup, H. P., Van Landeghem, K. J. J., and Wilson, P.: Growth and retreat of the last British–Irish Ice Sheet, 31 000 to 15 000 years ago: the BRITICE-CHRONO reconstruction,  
1592 *Boreas*, 51, 699–758, <https://doi.org/10.1111/bor.12594>, 2022.
- 1594 Cogež, A., Herman, F., Pelt, É., Reuschlé, T., Morvan, G., Darvill, C. M., Norton, K. P., Christl, M., Märki, L., and Chabaux, F.: U-Th and <sup>10</sup>Be constraints on sediment recycling in proglacial settings, Lago Buenos Aires, Patagonia, *Earth Surface Dynamics*, 6, 121–140, <https://doi.org/10.5194/esurf-6-121-2018>, 2018.
- 1598 Cook, S. J., Swift, D. A., Kirkbride, M. P., Knight, P. G., and Waller, R. I.: The empirical basis for modelling glacial erosion rates, *Nat. Commun.*, 11, 1–7, <https://doi.org/10.1038/s41467-020-14583-8>, 2020.



- 1600 Cordonnier, G., Jouvét, G., Peytavie, A., Braun, J., Cani, M.-P., Benes, B., Galin, E., Guérin, E., and Gain, J.: Forming Terrains by Glacial Erosion, *ACM Trans. Graph.*, 42, 1–14, <https://doi.org/10.1145/3592422>, 2023.
- 1602 Coutterand, S.: Étude géomorphologique des flux glaciaires dans les Alpes nord-occidentales au Pléistocène récent. Du maximum de la dernière glaciation aux premières étapes de la déglaciation., PhD thesis, Université de Savoie, Le Bourget du Lac, 1–468 pp., 2010.
- 1604 Coutterand, S.: Origines des blocs erratiques du Salève, *Arch. Sci.*, 70, 51–56, 2018.
- Cuffey, K. M. and Patterson, W. S. B.: The physics of glaciers, Academic Press, 1–704 pp., 2010.
- 1606 Davies, B. J., Roberts, D. H., Bridgland, D. R., Ó Cofaigh, C., Riding, J. B., Demarchi, B., Penkman, K. E. H., and Pawley, S. M.: Timing and depositional environments of a Middle Pleistocene glaciation of northeast England: New evidence from Warren House Gill, County Durham, *Quat. Sci. Rev.*, 44, 180–212, <https://doi.org/10.1016/j.quascirev.2010.02.003>, 2012.
- 1610 Davies, B. J., Darvill, C. M., Lovell, H., Bendle, J. M., Dowdeswell, J. A., Fabel, D., García, J.-L., Geiger, A., Glasser, N. F., Gheorghiu, D. M., Harrison, S., Hein, A. S., Kaplan, M. R., Martin, J. R. V., Mendelova, M., Palmer, A., Pelto, M., Rodés, Á., Sagredo, E. A., Smedley, R. K., Smellie, J. L., and Thorndycraft, V. R.: The evolution of the Patagonian Ice Sheet from 35 ka to the present day (PATICE), *Earth. Sci. Rev.*, 204, 103152, <https://doi.org/10.1016/j.earscirev.2020.103152>, 2020.
- 1614 Delaney, I. and Anderson, L. S.: Debris Cover Limits Subglacial Erosion and Promotes Till Accumulation, *Geophys. Res. Lett.*, 49, <https://doi.org/10.1029/2022GL099049>, 2022.
- 1618 Delaney, I., Anderson, L., and Herman, F.: Modeling the spatially distributed nature of subglacial sediment transport and erosion, *Earth Surface Dynamics*, 11, 663–680, <https://doi.org/10.5194/esurf-11-663-2023>, 2023.
- 1620 Dielforder, A. and Hetzel, R.: The deglaciation history of the Simplon region (southern Swiss Alps) constrained by <sup>10</sup>Be exposure dating of ice-molded bedrock surfaces, *Quat. Sci. Rev.*, 84, 26–38, <https://doi.org/10.1016/j.quascirev.2013.11.008>, 2014.
- 1622 Duprat-Oualid, F., Rius, D., Bégeot, C., Magny, M., Millet, L., Wulf, S., and Appelt, O.: Vegetation response to abrupt climate changes in Western Europe from 45 to 14.7k cal a BP: the Bergsee lacustrine record (Black Forest, Germany), *J. Quat. Sci.*, 32, 1008–1021, <https://doi.org/10.1002/jqs.2972>, 2017.
- 1624 Egholm, D. L., Knudsen, M. F., Clark, C. D., and Lesemann, J. E.: Modeling the flow of glaciers in steep terrains: The integrated second-order shallow ice approximation (iSOSIA), *J. Geophys. Res. Earth Surf.*, 116, <https://doi.org/10.1029/2010JF001900>, 2011.
- 1626 Ehlers, J., Gibbard, P. L., and Hughes, P. D.: Developments in quaternary sciences: quaternary glaciations-extent and chronology: a closer look, 1st ed., edited by: Ehlers, J., Gibbard, P. L., and Hughes, P. D., Elsevier, Amsterdam, 2–1118 pp., 2011.
- 1630 Ely, J. C., Clark, C. D., Small, D., and Hindmarsh, R. C. A.: ATAT 1.1, the Automated Timing Accordance Tool for comparing ice-sheet model output with geochronological data, *Geosci. Model Dev.*, 12, 933–953, <https://doi.org/10.5194/gmd-12-933-2019>, 2019.
- 1632 Enkelmann, E. and Ehlers, T. A.: Evaluation of detrital thermochronology for quantification of glacial catchment denudation and sediment mixing, *Chem. Geol.*, 411, 299–309, <https://doi.org/10.1016/j.chemgeo.2015.07.018>, 2015.
- 1636 Esmark, J.: Bidrag til vor Jordklodes Historie, *Magazin for Naturvidenskaberne*, 2, 28–49, 1824.
- 1638 Evans, D. J. A. and Benn, D. I.: A Practical Guide to the Study of Glacial Sediments, Routledge, 2004.
- 1640 Evans, D. J. A., Phillips, E. R., Hiemstra, J. F., and Auton, C. A.: Subglacial till: Formation, sedimentary characteristics and classification, *Earth. Sci. Rev.*, 78, 115–176, <https://doi.org/10.1016/j.earscirev.2006.04.001>, 2006.



- 1642 Federici, P. R., Ribolini, A., and Spagnolo, M.: Glacial history of the Maritime Alps from the Last Glacial  
Maximum to the Little Ice Age, *Geological Society, London, Special Publications*, 433, 137–159,  
1644 <https://doi.org/10.1144/SP433.9>, 2017.
- Fedotova, A. and Magnani, M. B.: Glacial Erosion Rates Since the Last Glacial Maximum for the Former  
1646 Argentino Glacier and Present-Day Upsala Glacier, Patagonia, *J. Geophys. Res. Earth Surf.*, 129,  
<https://doi.org/10.1029/2024JF007960>, 2024.
- 1648 Fischer, L., Purves, R. S., Huggel, C., Noetzli, J., and Haeberli, W.: On the influence of topographic, geological  
and cryospheric factors on rock avalanches and rockfalls in high-mountain areas, *Natural Hazards and Earth  
1650 System Sciences*, 12, 241–254, <https://doi.org/10.5194/nhess-12-241-2012>, 2012.
- Fischer, U. H., Bebiolka, A., Brandefelt, J., Follin, S., Hirschorn, S., Jensen, M., Keller, S., Kennell, L., Näslund,  
1652 J.-O., Normani, S., Selroos, J.-O., and Vidstrand, P.: Radioactive Waste Under Conditions of Future Ice Ages, in:  
Snow and Ice-Related Hazards, Risks, and Disasters, edited by: Shroder, J. F., Haeberli, W., and Whiteman, C.,  
1654 Elsevier, Boston, 345–393, <https://doi.org/10.1016/B978-0-12-394849-6.00011-1>, 2015.
- Fischer, U. H., Bebiolka, A., Brandefelt, J., Cohen, D., Harper, J., Hirschorn, S., Jensen, M., Kennell, L., Liakka,  
1656 J., Näslund, J.-O., Normani, S., Stück, H., and Weitkamp, A.: Radioactive waste under conditions of future ice  
ages, in: *Snow and Ice-Related Hazards, Risks, and Disasters*, edited by: Haeberli, W. and Whiteman, C., Elsevier,  
1658 323–375, <https://doi.org/10.1016/B978-0-12-817129-5.00005-6>, 2021.
- Florineth, D. and Schlüchter, C.: Reconstructing the Last Glacial Maximum (LGM) ice surface geometry and  
1660 flowlines in the Central Swiss Alps, *Eclogae Geologicae Helvetiae*, 91, <https://doi.org/10.5169/seals-168431>,  
1998.
- 1662 Gallach, X., Perrette, Y., Lafon, D., Chalmin, É., Deline, P., Ravanel, L., Carcaillet, J., and Wallet, T.: A new  
method for dating the surface exposure age of granite rock walls in the Mont Blanc massif by reflectance  
1664 spectroscopy, *Quat. Geochronol.*, 64, 101–156, <https://doi.org/10.1016/j.quageo.2021.101156>, 2021.
- Geikie, J.: The Alps during the Glacial Period, *Bulletin of the American Geographical Society*, 42, 192,  
1666 <https://doi.org/10.2307/200422>, 1910.
- Geologische Bundesanstalt Österreich: Geodaten - Blatt 197 Kötschach (1:50.000), Tethys RDR, Geologische  
1668 Bundesanstalt (GBA), Wien, <https://doi.org/https://doi.org/10.24341/tethys.90>, 2021a.
- Geologische Bundesanstalt Österreich: Geodaten - Blatt 198 Weißbriach (1:50.000), Tethys RDR, Geologische  
1670 Bundesanstalt (GBA), Wien, <https://doi.org/https://doi.org/10.24341/tethys.88>, 2021b.
- Gianotti, F., Forno, M. G., Ivy-Ochs, S., and Kubik, P. W.: New chronological and stratigraphical data on the Ivrea  
1672 amphitheatre (Piedmont, NW Italy), *Quaternary International*, 190, 123–135,  
<https://doi.org/10.1016/j.quaint.2008.03.001>, 2008.
- 1674 Gianotti, F., Forno, M. G., Ajassa, R., Cámara, F., Costa, E., Ferrando, S., Giardino, M., Lucchesi, S., Motta, L.,  
Motta, M., Perotti, L., and Rossetti, P.: The Ivrea Morainic Amphitheatre as a Well Preserved Record of the  
1676 Quaternary Climate Variability (PROGEO-Piemonte Project, NW Italy), in: *Engineering Geology for Society and  
Territory - Volume 8*, edited by: Lollino Giorgio and Giordan, D. and M. C. and C. B. and Y. I. and M. C.,  
1678 Springer International Publishing, Cham, 235–238, [https://doi.org/10.1007/978-3-319-09408-3\\_39](https://doi.org/10.1007/978-3-319-09408-3_39), 2015.
- Gibbons, A. B., Megeath, Joe. D., and Pierce, K. L.: Probability of moraine survival in a succession of glacial  
1680 advances, *Geology*, 12, 327, [https://doi.org/10.1130/0091-7613\(1984\)12<327:POMSIA>2.0.CO;2](https://doi.org/10.1130/0091-7613(1984)12<327:POMSIA>2.0.CO;2), 1984.
- Glasser, N. and Jansson, K.: The Glacial map of southern South America, *J. Maps*, 4, 175–196,  
1682 <https://doi.org/10.4113/jom.2008.1020>, 2008.
- Graf, A., Akçar, N., Ivy-Ochs, S., Strasky, S., Kubik, P. W., Christl, M., Burkhard, M., Wieler, R., and Schlüchter,  
1684 C.: Multiple advances of Alpine glaciers into the Jura Mountains in the Northwestern Switzerland, *Swiss J.  
Geosci.*, 108, 225–238, <https://doi.org/10.1007/s00015-015-0195-y>, 2015.



- 1686 Guillon, H., Mugnier, J., Buoncristiani, J., Carcaillet, J., Godon, C., Prud'homme, C., van der Beek, P., and Vassallo, R.: Improved discrimination of subglacial and periglacial erosion using 10Be concentration
- 1688 measurements in subglacial and supraglacial sediment load of the Bossons glacier (Mont Blanc massif, France), *Earth Surf. Process. Landf.*, 40, 1202–1215, <https://doi.org/10.1002/esp.3713>, 2015.
- 1690 Hallet, B.: Glacial Abrasion and Sliding: their Dependence on the Debris Concentration in Basal Ice, *Ann. Glaciol.*, 2, 23–28, <https://doi.org/10.3189/172756481794352487>, 1981.
- 1692 Herman, F., Beyssac, O., Brughelli, M., Lane, S. N., Leprince, S., Adatte, T., Lin, J. Y. Y., Avouac, J.-P., and Cox, S. C.: Erosion by an Alpine glacier, *Science* (1979)., 350, 193–195, <https://doi.org/10.1126/science.aab2386>,
- 1694 2015.
- Herman, F., De Doncker, F., Delaney, I., Prasicek, G., and Koppes, M.: The impact of glaciers on mountain erosion, *Nat. Rev. Earth Environ.*, 2, 422–435, <https://doi.org/10.1038/s43017-021-00165-9>, 2021.
- 1698 Heyman, J., Stroeven, A. P., Harbor, J. M., and Caffee, M. W.: Too young or too old: Evaluating cosmogenic exposure dating based on an analysis of compiled boulder exposure ages, *Earth Planet. Sci. Lett.*, 302, 71–80, <https://doi.org/10.1016/j.epsl.2010.11.040>, 2011.
- 1700 Hughes, A. L. C., Clark, C. D., and Jordan, C. J.: Subglacial bedforms of the last British Ice sheet, *J. Maps*, 6, 543–563, <https://doi.org/10.4113/jom.2010.1111>, 2010.
- 1702 Humlum, O.: Changes in Texture and Fabric of Particles in Glacial Traction with Distance from Source, Mýrdalsjökull, Iceland, *Journal of Glaciology*, 31, 150–156, <https://doi.org/10.3189/S002214300006390>, 1985.
- 1704 Humphrey, N. F. and Raymond, C. F.: Hydrology, erosion and sediment production in a surging glacier: Variegated Glacier, Alaska, 1982–83, *Journal of Glaciology*, 40, 539–552,
- 1706 <https://doi.org/10.3189/S0022143000012429>, 1994.
- van Husen, D.: LGM and late-glacial fluctuations in the Eastern Alps, *Quaternary International*, 38–39, 109–118,
- 1708 [https://doi.org/10.1016/S1040-6182\(96\)00017-1](https://doi.org/10.1016/S1040-6182(96)00017-1), 1997.
- Iverson, N. R., Hanson, B., Hooke, R. LeB., and Jansson, P.: Flow Mechanism of Glaciers on Soft Beds, *Science* (1979)., 267, 80–81, <https://doi.org/10.1126/science.267.5194.80>, 1995.
- 1710 Iverson, N. R., Cohen, D., Hooyer, T. S., Fischer, U. H., Jackson, M., Moore, P. L., Lappégard, G., and Kohler, J.: Effects of Basal Debris on Glacier Flow, *Science* (1979)., 301, 81–84, <https://doi.org/10.1126/science.1083086>,
- 1712 2003.
- 1714 Ivy-Ochs, S.: Glacier variations in the European Alps at the end of the last glaciation, *Cuadernos de Investigación Geográfica*, 41, 295–315, <https://doi.org/10.18172/cig.2750>, 2015.
- 1716 Ivy-Ochs, S., Schäfer, J., Kubik, P. W., Synal, H. A., and Schlüchter, C.: Timing of deglaciation on the northern Alpine foreland (Switzerland), *Eclogae Geologicae Helvetiae*, 97, 47–55, <https://doi.org/10.1007/s00015-004-1110-0>, 2004.
- 1718 Ivy-Ochs, S., Lucchesi, S., Baggio, P., Fioraso, G., Gianotti, F., Monegato, G., Graf, A. A., Akçar, N., Christl, M., Carraro, F., Forno, M. G., and Schlüchter, C.: New geomorphological and chronological constraints for glacial deposits in the Rivoli-Avigliana end-moraine system and the lower Susa Valley (Western Alps, NW Italy), *J. Quat. Sci.*, 33, 550–562, <https://doi.org/10.1002/jqs.3034>, 2018.
- 1720 Ivy-Ochs, S., Monegato, G., and Reitner, J. M.: The Alps: glacial landforms from the Last Glacial Maximum, in: *European Glacial Landscapes*, edited by: Palacios, D., Hughes, P. D., García-Ruiz, J. M., and Andrés, N., Elsevier, 449–460, <https://doi.org/10.1016/B978-0-12-823498-3.00030-3>, 2022.
- 1724 Jain, A., Kerbl, B., Gain, J., Finley, B., and Cordonnier, G.: FastFlow: GPU Acceleration of Flow and Depression Routing for Landscape Simulation, *Computer Graphics Forum*, 43, <https://doi.org/10.1111/cgf.15243>, 2024.
- 1726



- 1728 Jouvét, G. and Cordonnier, G.: Ice-flow model emulator based on physics-informed deep learning, *Journal of Glaciology*, 1–15, <https://doi.org/10.1017/jog.2023.73>, 2023.
- 1730 Jouvét, G., Seguinot, J., Ivy-ochs, S., and Funk, M.: Modelling the diversion of erratic boulders by the Valais Glacier during the last glacial maximum, *Journal of Glaciology*, 63, 487–498, <https://doi.org/10.1017/jog.2017.7>,  
1732 2017.
- Jouvét, G., Cordonnier, G., Kim, B., Lüthi, M., Vieli, A., and Aschwanden, A.: Deep learning speeds up ice flow  
1734 modelling by several orders of magnitude, *Journal of Glaciology*, 68, 651–664,  
<https://doi.org/10.1017/jog.2021.120>, 2022.
- 1736 Jouvét, G., Cohen, D., Russo, E., Buzan, J., Raible, C. C., Haeberli, W., Kamleitner, S., Ivy-Ochs, S., Imhof, M.  
A., Becker, J. K., Landgraf, A., and Fischer, U. H.: Coupled climate-glacier modelling of the last glaciation in the  
1738 Alps, *Journal of Glaciology*, 1–15, <https://doi.org/10.1017/jog.2023.74>, 2023.
- Kamleitner, S., Ivy-Ochs, S., Monegato, G., Gianotti, F., Akçar, N., Vockenhuber, C., Christl, M., and Synal, H.-  
1740 A.: The Ticino-Toce glacier system (Swiss-Italian Alps) in the framework of the Alpine Last Glacial Maximum,  
*Quat. Sci. Rev.*, 279, 107400, <https://doi.org/10.1016/j.quascirev.2022.107400>, 2022.
- 1742 Kamleitner, S., Ivy-Ochs, S., Manatschal, L., Akçar, N., Christl, M., Vockenhuber, C., Hajdas, I., and Synal, H.-  
A.: Last Glacial Maximum glacier fluctuations on the northern Alpine foreland: Geomorphological and  
1744 chronological reconstructions from the Rhine and Reuss glacier systems, *Geomorphology*, 423, 108548,  
<https://doi.org/10.1016/j.geomorph.2022.108548>, 2023.
- 1746 Kamleitner, S., Leger, T. P. M., Ivy-Ochs, S., Nussbaumer, S. U., Vieli, A., and Jouvét, G.: AlpIce - Towards an  
Alps-wide database of empirical geo(morpho)logical and geochronological data constraining Last Glacial  
1748 Maximum to Holocene glacier fluctuations, in: EGU General Assembly 2024, <https://doi.org/10.5194/egusphere-egu24-9282>, 2024a.
- 1750 Kamleitner, S., Ivy-Ochs, S., Salcher, B., and Reitner, J. M.: Reconstructing basal ice flow patterns of the Last  
Glacial Maximum Rhine glacier (northern Alpine foreland) based on streamlined subglacial landforms, *Earth  
1752 Surf. Process. Landf.*, 49, 746–769, <https://doi.org/10.1002/esp.5733>, 2024b.
- Keller, O. and Krayss, E.: Mittel- und spätpleistozäne Stratigraphie und Morphogenese in Schlüsselregionen der  
1754 Nordschweiz, *E&G Quaternary Science Journal*, 59, 88–119, <https://doi.org/10.3285/eg.59.1-2.08>, 2011.
- Kelly, M. A., Buoncristiani, J.-F., and Schlüchter, C.: A reconstruction of the last glacial maximum (LGM) ice-  
1756 surface geometry in the western Swiss Alps and contiguous Alpine regions in Italy and France, *Eclogae  
Geologicae Helvetiae*, 97, 57–75, <https://doi.org/10.1007/s00015-004-1109-6>, 2004.
- 1758 Koppes, M., Hallet, B., Rignot, E., Mouginot, J., Wellner, J. S., and Boldt, K.: Observed latitudinal variations in  
erosion as a function of glacier dynamics, *Nature*, 526, 100–103, <https://doi.org/10.1038/nature15385>, 2015.
- 1760 Lane, S. N., Bakker, M., Gabbud, C., Micheletti, N., and Saugy, J.-N.: Sediment export, transient landscape  
response and catchment-scale connectivity following rapid climate warming and Alpine glacier recession,  
1762 *Geomorphology*, 277, 210–227, <https://doi.org/10.1016/j.geomorph.2016.02.015>, 2017.
- Leger, T. P. M., Jouvét, G., Kamleitner, S., Mey, J., Herman, F., Finley, B. D., Ivy-Ochs, S., Vieli, A., Henz, A.,  
1764 and Nussbaumer, S. U.: A data-consistent model of the last glaciation in the Alps achieved with physics-driven AI,  
*Nat. Commun.*, 16, 848, <https://doi.org/10.1038/s41467-025-56168-3>, 2025.
- 1766 Lehner, B. and Grill, G.: Global river hydrography and network routing: baseline data and new approaches to  
study the world's large river systems, *Hydrol. Process.*, 27, 2171–2186, <https://doi.org/10.1002/hyp.9740>, 2013.
- 1768 Letsch, D., Winkler, W., von Quadt, A., and Gallhofer, D.: The volcano-sedimentary evolution of a post-Variscan  
intramontane basin in the Swiss Alps (Glarus Verrucano) as revealed by zircon U–Pb age dating and Hf isotope  
1770 geochemistry, *International Journal of Earth Sciences*, 104, 123–145, <https://doi.org/10.1007/s00531-014-1055-0>,  
2015.



- 1772 Linton, D. L.: Watershed Breaching by Ice in Scotland, *Transactions and Papers (Institute of British Geographers)*, 1, <https://doi.org/10.2307/621028>, 1949.
- 1774 Luetscher, M., Boch, R., Sodemann, H., Spötl, C., Cheng, H., Edwards, R. L., Frisia, S., Hof, F., and Müller, W.: North Atlantic storm track changes during the Last Glacial Maximum recorded by Alpine speleothems, *Nat. Commun.*, 6, 6344, <https://doi.org/10.1038/ncomms7344>, 2015.
- 1776 Lyell, C.: On the geological evidence of the former existence of glaciers in Forfarshire, *Proceedings of the Geological Society of London*, 3, 337–345, 1840.
- 1778 Manzotti, P.: Petro-structural map of the Dent Blanche tectonic system between Valpelline and Valtournenche valleys, *Western Italian Alps*, *J. Maps*, 7, 340–352, <https://doi.org/10.4113/jom.2011.1179>, 2011.
- 1782 Margirier, A., Brondex, J., Rowan, A. V., Schmidt, C., Pedersen, V. K., Lehmann, B., Anderson, L. S., Veness, R., Watson, C. S., Swift, D., and King, G. E.: Tracking Sediment Transport Through Miage Glacier, Italy, Using a Lagrangian Approach With Luminescence Rock Surface Burial Dating of Englacial Clasts, *J. Geophys. Res. Earth Surf.*, 130, <https://doi.org/10.1029/2024JF007773>, 2025.
- 1784 Matthews, J. A., Shakesby, R. A., and Fabel, D.: Very low inheritance in cosmogenic surface exposure ages of glacial deposits: A field experiment from two Norwegian glacier forelands, *Holocene*, 27, 1406–1414, <https://doi.org/10.1177/0959683616687387>, 2017.
- 1788 Mey, J., Scherler, D., Wickert, A. D., Egholm, D. L., Tesauero, M., Schildgen, T. F., and Strecker, M. R.: Glacial isostatic uplift of the European Alps, *Nat. Commun.*, 7, 13382, <https://doi.org/10.1038/ncomms13382>, 2016.
- 1790 Mohammadi, M., McMackin, C., and Egli, M.: Source identification of morainic materials in soils of the Three Lakes region (Switzerland) using the fingerprinting technique, *Catena (Amst.)*, 234, 107619, <https://doi.org/10.1016/j.catena.2023.107619>, 2024.
- 1792 Monegato, G., Scardia, G., Hajdas, I., Rizzini, F., and Piccin, A.: The Alpine LGM in the boreal ice-sheets game, *Sci. Rep.*, 7, 2078, <https://doi.org/10.1038/s41598-017-02148-7>, 2017.
- 1796 Monegato, G., Kamleitner, S., Gianotti, F., Martin, S., Scapozza, C., and Ivy-Ochs, S.: The Ticino-Toce Ice Conveyor Belts During The Last Glacial Maximum, *Alpine and Mediterranean Quaternary*, 35, 119–134, <https://doi.org/https://doi.org/10.26382/AMQ.2022.07>, 2022.
- 1798 Moosdorf, N., Cohen, S., and von Hagke, C.: A global erodibility index to represent sediment production potential of different rock types, *Applied Geography*, 101, 36–44, <https://doi.org/10.1016/j.apgeog.2018.10.010>, 2018.
- 1800 Overeem, I., Hudson, B. D., Syvitski, J. P. M., Mikkelsen, A. B., Hasholt, B., van den Broeke, M. R., Noël, B. P. Y., and Morlighem, M.: Substantial export of suspended sediment to the global oceans from glacial erosion in Greenland, *Nat. Geosci.*, 10, 859–863, <https://doi.org/10.1038/ngeo3046>, 2017.
- 1802 Penck, A. and Brückner, E.: *Die Alpen im Eiszeitalter*, Tauchnitz, 1909.
- 1804 Preusser, F., Reitner, J. M., and Schlüchter, C.: Distribution, geometry, age and origin of overdeepened valleys and basins in the Alps and their foreland, *Swiss J. Geosci.*, 103, 407–426, <https://doi.org/10.1007/s00015-010-0044-y>, 2010.
- 1806 Preusser, F., Graf, H. R., Keller, O., Krayss, E., and Schlüchter, C.: Quaternary glaciation history of northern Switzerland, *E&G Quaternary Science Journal*, 60, 282–305, <https://doi.org/10.3285/eg.60.2-3.06>, 2011.
- 1808 Prud'homme, C., Vassallo, R., Crouzet, C., Carcaillet, J., Mugnier, J., and Cortés-Aranda, J.: Paired 10Be sampling of polished bedrock and erratic boulders to improve dating of glacial landforms: an example from the Western Alps, *Earth Surf. Process. Landf.*, 45, 1168–1180, <https://doi.org/10.1002/esp.4790>, 2020.
- 1810 Ravazzi, C., Badino, F., Marsetti, D., Patera, G., and Reimer, P. J.: Glacial to paraglacial history and forest recovery in the Oglio glacier system (Italian Alps) between 26 and 15 ka cal BP, *Quat. Sci. Rev.*, 58, 146–161, <https://doi.org/10.1016/j.quascirev.2012.10.017>, 2012.
- 1814



- 1816 Reber, R., Akçar, N., Ivy-Ochs, S., Tikhomirov, D., Burkhalter, R., Zahno, C., Lüthold, A., Kubik, P. W., Vockenhuber, C., and Schlüchter, C.: Timing of retreat of the Reuss Glacier (Switzerland) at the end of the Last Glacial Maximum, *Swiss J. Geosci.*, 107, 293–307, <https://doi.org/10.1007/s00015-014-0169-5>, 2014.
- 1818 Reitner, J. M.: Glacial dynamics at the beginning of Termination I in the Eastern Alps and their stratigraphic implications, *Quaternary International*, 164–165, 64–84, <https://doi.org/10.1016/j.quaint.2006.12.016>, 2007.
- 1820 Reitner, J. M., Gruber, W., Römer, A., and Morawetz, R.: Alpine overdeepenings and paleo-ice flow changes: an integrated geophysical-sedimentological case study from Tyrol (Austria), *Swiss J. Geosci.*, 103, 385–405, 1822 <https://doi.org/10.1007/s00015-010-0046-9>, 2010.
- 1824 Reynard, E.: Protecting stones: conservation of erratic blocks in Switzerland, in: *Dimension stone*, Taylor and Francis, London, 3–7, 2004.
- 1826 Ribolini, A., Spagnolo, M., Cyr, A. J., and Federici, P. R.: Last Glacial Maximum and early deglaciation in the Stura Valley, southwestern European Alps, *Quat. Sci. Rev.*, 295, 107770, <https://doi.org/10.1016/j.quascirev.2022.107770>, 2022.
- 1828 Roattino, T., Crouzet, C., Vassallo, R., Buoncristiani, J. F., Carcaillet, J., Gribenski, N., and Valla, P. G.: Paleogeographical reconstruction of the western French Alps foreland during the last glacial maximum using 1830 cosmogenic exposure dating, *Quaternary Research (United States)*, 111, 68–83, <https://doi.org/10.1017/qua.2022.25>, 2023.
- 1832 Rowan, A. V., Egholm, D. L., Quincey, D. J., and Glasser, N. F.: Modelling the feedbacks between mass balance, ice flow and debris transport to predict the response to climate change of debris-covered glaciers in the Himalaya, 1834 *Earth Planet. Sci. Lett.*, 430, 427–438, <https://doi.org/10.1016/j.epsl.2015.09.004>, 2015.
- 1836 Russo, E., Buzan, J., Lienert, S., Juvet, G., Velasquez Alvarez, P., Davis, B., Ludwig, P., Joos, F., and Raible, C. C.: High-resolution LGM climate of Europe and the Alpine region using the regional climate model WRF, *Climate of the Past*, 20, 449–465, <https://doi.org/10.5194/cp-20-449-2024>, 2024.
- 1838 Rybak, O. and Huybrechts, P.: A comparison of Eulerian and Lagrangian methods for dating in numerical ice-sheet models, *Ann. Glaciol.*, 37, 150–158, <https://doi.org/10.3189/172756403781815393>, 2003.
- 1840 Scherler, D. and Egholm, D. L.: Production and Transport of Supraglacial Debris: Insights From Cosmogenic 10Be and Numerical Modeling, *Chhota Shigri Glacier, Indian Himalaya, J. Geophys. Res. Earth Surf.*, 125, 1842 <https://doi.org/10.1029/2020JF005586>, 2020.
- 1844 Schoof, C. and Hewitt, I.: Ice-Sheet Dynamics, *Annu. Rev. Fluid Mech.*, 45, 217–239, <https://doi.org/10.1146/annurev-fluid-011212-140632>, 2013.
- 1846 Seguinot, J. and Delaney, I.: Last-glacial-cycle glacier erosion potential in the Alps, *Earth Surface Dynamics*, 9, 923–935, <https://doi.org/10.5194/esurf-9-923-2021>, 2021.
- 1848 Seguinot, J., Ivy-Ochs, S., Juvet, G., Huss, M., Funk, M., and Preusser, F.: Modelling last glacial cycle ice dynamics in the Alps, *Cryosphere*, 12, 3265–3285, <https://doi.org/10.5194/tc-12-3265-2018>, 2018.
- 1850 Small, R. J., Clark, M. J., and Cawse, T. J. P.: The Formation of Medial Moraines on Alpine Glaciers, *Journal of Glaciology*, 22, 43–52, <https://doi.org/10.3189/S0022143000014040>, 1979.
- 1852 Sugden, David. E. and John, Brian. S.: *Glaciers and Landscape: A Geomorphological Approach*, 1st ed., Edward Arnold, London, 1–376 pp., 1976.
- 1854 Tadono, T., Ishida, H., Oda, F., Naito, S., Minakawa, K., and Iwamoto, H.: Precise Global DEM Generation by ALOS PRISM, *ISPRS Annals of the Photogrammetry, Remote Sensing and Spatial Information Sciences*, II–4, 71–76, <https://doi.org/10.5194/isprsannals-II-4-71-2014>, 2014.
- 1856 Valla, P. G., Shuster, D. L., and van der Beek, P. A.: Significant increase in relief of the European Alps during mid-Pleistocene glaciations, *Nat. Geosci.*, 4, 688–692, <https://doi.org/10.1038/ngeo1242>, 2011.



- 1858 Veness, R. L., Clark, C. D., Ely, J. C., Knight, J. L., Igneczi, A., and Bradley, S. L.: Modelling erratic dispersal  
accounting for shifting ice flow geometries: A new method and explanations of erratic dispersal of the British–  
1860 Irish Ice Sheet, *J. Quat. Sci.*, <https://doi.org/10.1002/jqs.3720>, 2025.
- Venez, I.: Sur l'ancienne extension des glaciers et sur leur retraite dans leur limites actuelles, in: Actes de la  
1862 Société Helvétique des Sciences Naturelles. Quinzieme Réunion Annuelle à l'Hospice du Grand-Saint-Bernard,  
21–22, 1830.
- 1864 Walder, J. S. and Fowler, A.: Channelized subglacial drainage over a deformable bed, *Journal of Glaciology*, 40,  
3–15, <https://doi.org/10.3189/S0022143000003750>, 1994.
- 1866 Wang, B., Wald, I., Morrical, N., Usher, W., Mu, L., Thompson, K., and Hughes, R.: An GPU-accelerated particle  
tracking method for Eulerian–Lagrangian simulations using hardware ray tracing cores, *Comput. Phys. Commun.*,  
1868 271, 108221, <https://doi.org/10.1016/j.cpc.2021.108221>, 2022.
- Wickert, A. D.: Open-source modular solutions for flexural isostasy: gFlex v1.0, *Geoscientific Model  
1870 Development Discussions*, 8, 4245–4292, <https://doi.org/10.5194/gmdd-8-4245-2015>, 2015.
- Wüthrich, L., Morabito, E. G., Zech, J., Trauerstein, M., Veit, H., Gnägi, C., Merchel, S., Scharf, A., Rugel, G.,  
1872 Christl, M., and Zech, R.:  $^{10}\text{Be}$  surface exposure dating of the last deglaciation in the Aare Valley, Switzerland,  
*Swiss J. Geosci.*, 111, 295–303, <https://doi.org/10.1007/s00015-018-0298-3>, 2018.
- 1874 Zhang, T., Li, D., East, A. E., Walling, D. E., Lane, S., Overeem, I., Beylich, A. A., Koppes, M., and Lu, X.:  
Warming-driven erosion and sediment transport in cold regions, *Nat. Rev. Earth Environ.*, 3, 832–851,  
1876 <https://doi.org/10.1038/s43017-022-00362-0>, 2022.